Available online at www.sciencedirect.com
ScienceDirect
European Journal of Mechanics B/Fluids 28 (2009) 1–36

Numerical analysis of a weighted-residual integral boundary-layer model for nonlinear dynamics of falling liquid films

Alexander Oron *, O. Gottlieb, Elena Novbari

Department of Mechanical Engineering, Technion-Israel Institute of Technology, Haifa 32000, Israel

Received 13 January 2007; received in revised form 25 November 2007; accepted 17 December 2007

Available online 15 February 2008

Abstract

The nonlinear dynamics of thin liquid films falling on a vertical plane is investigated numerically using the first-order time-dependent weighted-residual integral boundary layer (WRIBL) equations derived by Ruyer-Quil and Manneville (2000). We validate the WRIBL equations by comparison of its solutions with those of its second-order version, solutions obtained by both stationary and time-dependent direct numerical simulation and experiments. We find that sufficiently close to the stability threshold of the system with periodic boundary conditions, the emerging waves are of γ_1-type. However, beyond a secondary bifurcation threshold, γ_2-type waves emerge and can coexist with γ_1-waves. The analysis of the WRIBL equations reveals, similar to the first-order Benney equation (BE), the existence of both periodic traveling wave (TW) and aperiodic non-stationary wave (NSW) flows. It is shown that although the WRIBL equations display bounded solutions for significantly larger values of the Reynolds number than the BE, they may exhibit negative flow rate which consists of reverse flow against gravity. The threshold for emergence of these solutions is a zero local flow rate that appears, for sufficiently large Kapitza numbers, to correspond to a specific value of the normalized wave height.

Keywords: Falling liquid films; Longwave theory; Nonlinear dynamics; Bifurcations

1. Introduction

Falling liquid films are often encountered in various technological applications, such as evaporators, condensers, heat exchangers, coating, and physical phenomena, such as gravity currents and lava flows. Significant progress has been attained in the analysis of thin (macroscopic) liquid films. Oron et al. [1] unified such analyses into a comprehensive framework in which the special cases naturally emerged. Employing the long-wave approximation Oron et al. [1] derived a generic evolution equation describing the spatio-temporal dynamics of a liquid film subjected to various physical mechanisms.

The long-wave approach has also been found to be a useful tool of investigation in the case when the base state is a flow and the Reynolds number of the flow is *not* large. An example is the dynamics of a liquid film flow on a vertical or inclined plane, where the steady Nusselt flow is known to be unstable to small long-wave disturbances.

* Corresponding author. Fax: +972 4 8295711.
E-mail address: meroron@tx.technion.ac.il (A. Oron).

0997-7546/$ – see front matter
doi:10.1016/j.euromechflu.2007.12.002

The Nusselt flow undergoes a Hopf bifurcation which evolves to temporal periodic or aperiodic waves, and the final selection depends on the flow parameter set and possibly the initial condition. In his pioneering work, Benney [2] derived the evolution equation referred nowadays as to the Benney equation (BE). This evolution equation describes the nonlinear dynamics of the interface of a two-dimensional liquid film flowing on a fixed inclined plane. The Benney equation in its dimensionless form can be written [3]

$$h_t + \frac{2}{3}(h^3)_x + \varepsilon\left[\left(\frac{8R}{15}h^6 - \cot\theta h^3\right)h_x + Wh^3h_{xxx}\right]_x = 0, \tag{1}$$

where $R = gd^3/\nu^2 \sin\theta$ is the unit-order Reynolds number of the flow driven by gravity g, $W = 2\varepsilon^2\sigma/(3\rho g d^2)$ is the rescaled inverse capillary number related to surface tension σ, θ is the angle of plane inclination with respect to the horizontal, ρ is the fluid density, d is the average film thickness, ν is the kinematic viscosity of the liquid, and ε represents the ratio between d and the wavelength of the characteristic interfacial disturbance λ. The independent variables x and t are rescaled non-dimensional spatial and temporal variables, respectively, and $h = h(x,t)$ is the local dimensionless thickness of the film scaled with d.

The Benney equation has been extensively studied over the years. Gjevik [3] introduced an approximate modal approach for a study of spatially periodic solutions of Eq. (1) Nakaya [4] constructed various traveling wave solutions for Eq. (1) in the infinite and periodic domains and investigated their properties. Salamon et al. [5] carried out the study of traveling waves on vertical films by solving the full *stationary*, i.e., steady in the moving frame of reference and describing traveling waves, hydrodynamic equations directly along with the free-surface boundary conditions using the finite element method. They also compared between some of these solutions with the traveling wave solutions of Eq. (1) and found a good agreement in certain domains. Direct numerical simulations of the Navier–Stokes equations for falling vertical liquid films were carried out by several groups [6–12]. Joo and Davis [13] showed in the BE that all two-dimensional saturated waves are unstable to two-dimensional spatially subharmonic disturbances in the downstream direction culminating in apparently chaotic dynamics. They also investigated [14] the three-dimensional version of the BE to find complex three-dimensional cross-stream patterns. Ramaswamy et al. [15] were the first to document a quasiperiodic wave regime in an exhaustive numerical investigation of the time-dependent Navier–Stokes equations for falling films. Gao et al. [7] recently obtained quasiperiodic solutions for the same parameters as employed by Ramaswamy et al. [15] using the volume of fluid numerical technique. However, the wave amplitude as obtained in their computations is significantly lower than in computations made in [15]. Oron and Gottlieb [16] solved the BE numerically and discovered that for certain parameter conditions the BE spontaneously exhibited aperiodic non-stationary waves for standard initial data. These non-stationary waves were found to correspond to multimode interactions which were later analyzed by Gottlieb and Oron [17] in a fourth-order complex-mode projection to yield simple quasiperiodic waves in a reduced eighth-order dynamical system. Gottlieb and Oron [17] also discovered coexisting traveling waves and non-stationary waves in their complex-mode projection of the BE. However, no evidence of coexisting solutions was found in the corresponding numerical investigation of the BE. We note that determination of coexisting attractors in the boundary value problems for partial differential equations of the evolution type involves an extremely difficult search in the infinite-dimensional functional space of spatially-dependent initial conditions.

However, along with the success of the Benney equation model to describe the dynamics of falling liquid films, there is a serious drawback. It was found that the solutions of the Benney equation grow without bound in a certain subdomain of the linearly unstable region of the system. In this case the BE loses its physical relevance. The feature of solutions blow-up for the Benney equation was first noticed by Pumir et al. [18] and further studied by Rosenau et al. [19] and Oron and Gottlieb [16], where the valid range of the Benney equation was mapped in the appropriate parameter space. Gottlieb and Oron [17] investigated the bifurcation structure near the blow-up and determined that it corresponds to a saddle-node bifurcation. This structure was later verified by Scheid et al. [20] in the analysis of a corresponding third-order ordinary differential equation deduced for an assumed traveling wave form. The primary bifurcation of the first- and second-order Benney equations was investigated by Lin [21] and Oron and Gottlieb [22], who also studied the issue of sideband instability of monochromatic traveling waves. Oron and Gottlieb [22] demonstrated that the asymptotic series leading to the derivation of the Benney equation may be poorly converging.

To overcome some of the drawbacks associated with the BE for fluids with large surface tension (large Kapitza number) several approaches were recently attempted. Ooshida [23] proposed a regularization of the BE based on Pade approximations to the flux term. An alternative approach was introduced by Ruyer-Quil and Manneville [24,25] extending the boundary-layer theory developed by Shkadov [26]. The Shkadov theory was shown [27,28] to be suc-

cessful in describing the dynamics of falling films on static vertical and inclined substrates for intermediate Reynolds numbers ($R < 300$). However, it failed to match the linear stability threshold of the system, as was derived by Benjamin [29] using Orr–Sommerfeld equations, by Yih [30] employing long-wave expansions, and which is strictly satisfied by the BE, Eq. (1). A thorough numerical study of periodic solutions for the Shkadov equations was recently carried out by Shkadov and Sisoev [31,32]. The theory developed by Ruyer-Quil and Manneville [24,25] for both first- and second-order approximations of the Navier–Stokes equations in the case of large Kapitza numbers can be classified as weighted-residual integral boundary layer (WRIBL) theory. It corrected the inability of the Shkadov model equations to match the linear stability threshold of the system and was found to yield bounded solutions for a larger range of Reynolds numbers than in the case of the BE. Recently, Scheid et al. [20] carried out the investigation of traveling wave solutions of the first-order WRIBL equations with various boundary conditions and compared them with those of the BE. However, the time-dependent evolution of the falling films, as described by the first-order WRIBL equations with periodic boundary conditions, has not yet been investigated. Very recently, Mudunuri and Balakotaiah [33] derived a new two-equation model similar to that of Ruyer-Quil and Manneville [24] but valid in a different asymptotic limit related to the Reynolds and Weber numbers.

Kapitza and Kapitza [34] were the first to report the appearance of random-like waves in the absence of a pulsing feed to the flow. These results motivated the experiments by Lacy et al. [35] who obtained chaotic-like progressing waves which they proposed to be due to small levels of noise present in the simulations. Additional experiments with falling films on vertical [36,37] and inclined [38–40] planar surfaces were carried out and the emergence of spatially-random and spatially-regular wave regimes was reported in the cases of both natural and upstream perturbed flows. Salamon et al. [5] showed a good agreement with Kapitzas' experiment with alcohol films where traveling wave patterns were observed. However, as their investigation was restricted to traveling-wave patterns, they were unable to match the experimental non-stationary waves observed by Kapitzas [34] for water films. Ramaswamy et al. [15] and Gao et al. [7] later matched these non-stationary patterns in their time-dependent direct numerical simulations. Ruyer-Quil and Manneville [24] demonstrated that both their first- and second-order approximations compared well with the alcohol experiments on a vertical plane [34]. However, only their second-order approximation compared well with the experimental observation of Liu and Gollub [38] in water–glycerin solution on an inclined plane.

The objective of this paper is to investigate the nonlinear dynamics of falling films on a vertical plane in the framework of the first-order *time-dependent* WRIBL equations augmented by periodic boundary conditions and to compare their solutions with the experiments and with the solutions of the BE, namely traveling waves [5,16,17] and aperiodic waves [16,17], and also with the results of the studies of the WRIBL equations derived for traveling wave solutions [20]. We note that the experimental work of both Kapitza and Kapitza [34] and Alekseenko et al. [36,37] depicts spatially periodic structures in a long stretch of the flow domain before they become unstable and evolve into three-dimensional structures. This observation enabled Pumir et al. [18], Joo and Davis [13,14], Salamon et al. [5], Ramaswamy et al. [15], Gao et al. [7], Oron and Gottlieb [16], Gottlieb and Oron [17], Shkadov and Sisoev [32], and Scheid et al. [20] to make use of periodic boundary conditions in their investigations of the dynamics of falling films.

The paper is organized as follows: Section 2 is devoted to the formulation of the governing equations, the boundary-value problem, and their basic properties. Section 3 deals with linear stability theory of the base state. Section 4 briefly describes the numerical method and analysis' techniques employed here to study the fully nonlinear regime of the film evolution. In Section 5 we validate the first-order WRIBL by comparison of its solutions to those obtained by: (i) its second-order time-dependent and time-independent counterparts, (ii) solutions obtained by time-dependent and time-independent numerical solutions of the Navier–Stokes equations, and (iii) experimental data. In Section 6 we discuss the results of the numerical analysis of the evolution equation describing the film dynamics falling on a vertical plane and the comparison with both the Navier–Stokes and Benney equations. Section 7 is devoted to the possibility of the emergence of reverse flows as the solutions of the WRIBL equations. Section 8 presents the concluding remarks and focuses on conjectures for future research.

2. Governing evolution equations

We consider a two-dimensional flow of an isothermal liquid film of the average thickness d on a solid planar surface tilted at the angle θ to the horizontal in the gravity field g. The relevant properties of the liquid are density ρ, kinematic viscosity ν and surface tension σ.

In order to analyze the spatio-temporal evolution of the film interface we employ here the first-order WRIBL evolution equations derived by Ruyer-Quil and Manneville [24] in the non-dimensional form

$$h_t + q_x = 0, \tag{2}$$

$$q_t = \frac{5}{6}h - \frac{5}{6}Bhh_x + \frac{5}{6}\kappa hh_{xxx} - \frac{5}{2}\frac{q}{h^2} - \frac{17}{7}\frac{qq_x}{h} + \frac{9}{7}\frac{q^2h_x}{h^2}. \tag{3}$$

Here $B = \cot\theta$, $h = h(x,t)$, $q = q(x,t)$ are, respectively, the local film thickness and the leading-order approximation of the volumetric flow rate

$$q = \int_0^h u\,dy. \tag{4}$$

Both h and q depend on the spatial coordinate along the solid plane x and time t, u is the leading-order longitudinal x-component of the non-dimensional flow field, y is the spatial direction normal to the wall, and κ is the Kapitza number given by

$$\kappa = \frac{\sigma}{\rho\nu^{4/3}(g\sin\theta)^{1/3}}. \tag{5}$$

Eqs. (2) and (3) are written in the dimensionless form, while the dimensionless spatial coordinate x and film thickness h, time t, the longitudinal fluid velocity component u and the flow rate q scale the corresponding physical variables in terms of viscous length $l_\nu = (\nu^2/g\sin\theta)^{1/3}$, viscous time $t_\nu = (\nu/g^2\sin^2\theta)^{1/3}$, viscous velocity $U_\nu = (\nu g\sin\theta)^{1/3}$ and the value $U_\nu l_\nu$, respectively. It is important to recall that Eqs. (2) and (3) are asymptotically valid in the parameter domain of $R = \mathrm{O}(1)$, $\varepsilon^2\kappa = \mathrm{O}(1)$, where $\varepsilon \ll 1$ is the measure of smallness of the disturbance wavenumber. Very recently, Mudunuri and Balakotaiah [33] derived a two-equation model of the same asymptotic order valid in a different parameter domain of $R = \mathrm{O}(1)$, $\varepsilon\kappa R^{-2/3} = \mathrm{O}(1)$.

Eqs. (2) and (3) are hereafter numerically solved with periodic boundary conditions for both h and q in the domain $0 \leqslant x \leqslant L$ and for various initial conditions; one of them, namely

$$h(x, t=0) \equiv h_0(x) = h_N + \delta\sin\left(\frac{2\pi x}{L}\right), \qquad q(x, t=0) \equiv q_0(x) = q_N \tag{6}$$

with $h_N = d/l_\nu$ and $\delta \ll 1$ referred to as a "standard" initial condition. The value of δ is typically varied between 0.05 and 0.1. Note that the boundary-value problem at hand, Eqs. (2), (3), (6) is governed by two parameters, one of which κ is a pure material property and the other, h_N is the dimensionless mean film thickness.

The values h_N and q_N appearing in Eq. (6) are related to the Reynolds number based on the maximal value of the film velocity

$$R = \frac{gd^3}{2\nu^2}\sin\theta \tag{7}$$

via

$$h_N = (2R)^{1/3}, \qquad q_N = \frac{1}{3}h_N^3, \tag{8}$$

respectively, the dimensionless mean film thickness and the volumetric flow rate of the base Nusselt flow.

In order to compare the results of our investigation with other work related to the case of a vertical plate available in the literature, it is important to relate between various values used elsewhere. Oron and Gottlieb [16] employed in their investigations of the first-order Benney equation the parameters R, the rescaled Weber number $\tilde{S} = 2\sigma/(3\rho g d^2)$, and the small order parameter ε defined as the ratio between the mean film thickness and the characteristic wavelength of the interfacial disturbance. We note that Salamon et al. [5] used the value of the Weber number, $W = \frac{3}{2}\tilde{S}$, whereas Scheid et al. [20] used the value of the Reynolds number based on the average film velocity, $Re = \frac{2}{3}R$, and the value of the fundamental wavenumber k corresponding to the size of the periodic domain of L. These values are related in addition to the relationships given in Eq. (8) by

$$L = \frac{2\pi}{k}, \quad \varepsilon = \frac{kh_N}{2\pi}, \quad \kappa = Wh_N^2. \tag{9}$$

The first observation that can be made on the basis of Eqs. (2) and (3) is that if their solution is a traveling wave (TW) moving with the speed c, $h = h(\xi)$, $q = q(\xi)$ with $\xi = x - ct$, then Eq. (2) implies that

$$q(\xi) = ch(\xi) + A, \tag{10}$$

where $A = q_N - ch_N$ is a constant. However, as will be demonstrated below, not all solutions of Eqs. (2) and (3) are TW. We note that non-stationary wave regimes were also obtained [13,15–17] in the BE.

Next, it is readily seen that if Eqs. (2) and (3) are subject to periodic boundary conditions in the domain $0 \leqslant x \leqslant L$ for both h and q, Eq. (2) implies a mass conservation law

$$\frac{d}{dt}\int_0^L h\,dx = 0, \quad \text{equivalent to} \quad \frac{1}{L}\int_0^L h\,dx = h_N \quad \text{for all } t. \tag{11}$$

Integrating Eq. (3) over the periodic domain $0 \leqslant x \leqslant L$ and applying integration by parts yields

$$\frac{d}{dt}\int_0^L q\,dx = \frac{5}{6}h_N L - \frac{5}{2}\int_0^L \frac{q}{h^2}\,dx + \frac{1}{14}\int_0^L \frac{q^2}{h^2}h_x\,dx. \tag{12}$$

A physical interpretation of this conservation law is yet unclear. However, when the flow regime is TW, and therefore Eq. (10) is satisfied, the term on the left-hand side and the last term of the right-hand side of Eq. (12) vanish, and Eq. (12) reduces to

$$\frac{1}{L}\int_0^L \frac{q}{h^2}\,dx = \frac{1}{3}h_N. \tag{13}$$

Eq. (13) can serve as an additional check for accuracy of the numerical investigation of Eqs. (2) and (3). Also, Eq. (13) is identically satisfied by the base state {Nusselt flow} $h = h_N$, $q = q_N$ whose linear stability is considered next.

3. Linear stability analysis

We linearize Eqs. (2) and (3) around the base state $h = h_N$, $q = q_N$ with $h = h_N + \bar{\delta}\bar{h}$, $q = q_N + \bar{\delta}\bar{q}$, $\bar{\delta} \ll 1$, and introduce normal mode perturbations in the form of

$$\bar{h} = \eta \exp(ikx + \omega t), \qquad \bar{q} = \zeta \exp(ikx + \omega t), \tag{14}$$

where $k = 2\pi n/L$ and ω are their wavenumber and complex growth rate, respectively, and n is the integer number of the harmonics. Substituting Eq. (14) into the linearized version of Eqs. (2) and (3) yields the dispersion relation

$$\omega^2 + \omega\left(\frac{5}{2h_N^2} + \frac{17}{7}ik\frac{q_N}{h_N}\right) + ik\left[\frac{5}{6} + \frac{5q_N}{h_N^3} + ik\left(\frac{9q_N^2}{7h_N^2} - \frac{5}{6}k^2\kappa h_N - \frac{5}{6}h_N B\right)\right] = 0. \tag{15}$$

The pair $k = 0$, $\omega = 0$ is one of the solutions for Eq. (15) that corresponds to a spatially uniform disturbance of the flat interface $h = h_N$. Such disturbance must be zero to warrant mass conservation and thus represents a trivial at *all* times solution for Orr–Sommerfeld equations. Therefore, the instability can set in only via Hopf bifurcation with a nonzero wavenumber, as expected from experimental observations of the system at hand. Assuming that one of the eigenvalues ω to be purely imaginary $\omega_1 = i\Omega$ and the other to be a general complex number $\omega_2 = \alpha + i\beta$, leads to the following values of the unknowns

$$\alpha = -\frac{5}{2h_N^2} < 0, \quad \Omega = -kh_N^2 < 0, \quad \beta = \frac{4}{21}kh_N^2. \tag{16}$$

The negative sign of α suggests that the second mode, corresponding to ω_2 is stable for all n. The negative sign of Ω suggests that the wave propagates in the downward direction, i.e., in the direction of positive x. The dimensionless wave celerity at the stability threshold of the system (critical frequency) is obtained from Eqs. (14) and (16) as

$$c = h_N^2. \tag{17}$$

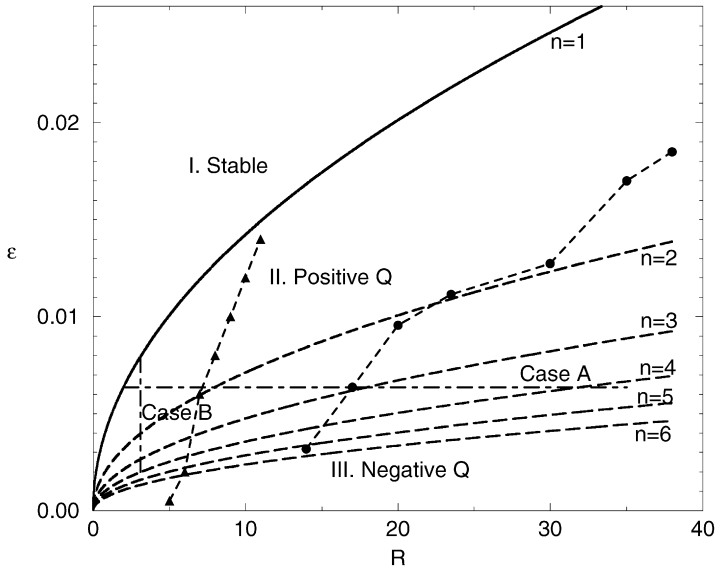

Fig. 1. Stability diagram for Eqs. (2) and (3) as presented in the ε–R plane. The curves $n = 1$ to $n = 6$ given by Eqs. (20), (21) show the instability thresholds for the n-th mode, thus $n = 1$ is the instability threshold of the system. The horizontal and vertical dot-dashed lines indicate the parameter values investigated here in the framework of cases A and B, respectively. The dashed curve marked with black circles displays the border line below which the value of Q becomes negative, while the line marked with black triangles represents the blowup line for the Benney equation, see the discussion in Section 7.

The stability threshold for the n-th mode is also obtained from Eqs. (15) and (16) in the form

$$R = R_n = \frac{5}{4}\left[\kappa\left(\frac{2n\pi}{L}\right)^2 + B\right], \quad n = 1, 2, \ldots, \tag{18}$$

and, in particular, the Hopf stability threshold of the system is given by

$$R = R_1 = \frac{5}{4}\left[\kappa\left(\frac{2\pi}{L}\right)^2 + B\right]. \tag{19}$$

Similarly, it follows from Eq. (18) that

$$\varepsilon_n = \frac{\varepsilon_1}{n}, \quad n = 1, 2, \ldots, \tag{20}$$

with

$$\varepsilon_1 = \frac{(2R_1)^{1/3}}{2\pi}\left[\left(\frac{4R_1}{5} - B\right)\Big/\kappa\right]^{1/2}. \tag{21}$$

It is important to note that Eqs. (19)–(21) is identical with the corresponding values of the stability threshold, as obtained for the Benney equation [16,17].

The linear stability threshold of the system given by Eq. (19) is also identical with that obtained directly from the Orr–Sommerfeld equations in the longwave limit [29]. If the period of the film is infinite, $L \to \infty$, it follows from Eq. (19) that the threshold of the instability is $R = \frac{5}{4}B$, also predicted by Benjamin [29] based on Orr–Sommerfeld equations. Note the difference in the definitions of the Reynolds number. The critical dimensionless wave speed given by Eq. (17) based on Eqs. (2) and (3) is also identical to that obtained by Benjamin [29] and both predict the dimensional wave speed of $gd^2 \sin\theta/\nu$.

Fig. 1 displays the stability diagram of the falling film for $W = 1000$. The curve $n = 1$ represents the Hopf stability threshold, as given by Eq. (21), and divides the ε–R plane into two domains, one of which (I), located above this curve is the domain of linear stability of the system, while the other (II and III combined), below the curve is that of its instability. The curves $n = 2$ to $n = 6$ show the stability thresholds of the respective n-th modes, as given by Eq. (20). Both, horizontal and vertical dot-dashed lines show the ranges, where our numerical investigation has been

carried out in cases A and B, respectively. The domain of the film instability, i.e. below the curve $n = 1$, is further subdivided into two subdomains II and III, where the boundary between these is the dashed line marked by black circles. The explanation of the dashed curves indicated by both the black circles and triangles will be given below, see Section 7.

4. Numerical technique and analyses methodology

The numerical technique used here to solve Eqs. (2) and (3) is based on the Newton–Kantorovich method, as described and implemented in [41,16]. The method employed there is now extended to handle a set of coupled equations (2) and (3).

Eqs. (2) and (3) are written in the form

$$\mathbf{y}_t = \mathbf{F}(\mathbf{y}), \tag{22}$$

where

$$\mathbf{y} = \begin{pmatrix} h(x,t) \\ q(x,t) \end{pmatrix}, \qquad \mathbf{F} = \begin{pmatrix} \mathbf{H}(h,q;x,t) \\ \mathbf{Q}(h,q;x,t) \end{pmatrix} \tag{23}$$

with $\mathbf{H} = -q_x$ and $\mathbf{Q}$ being given by the right-hand side of Eq. (3). To ensure the second-order accuracy of the solution in time we use the second-order, $(\mathrm{O}(\Delta t^2))$, accurate Runge–Kutta method

$$\mathbf{y}^{(n+1)} = \mathbf{y}^{(n)} + \frac{1}{2}\Delta t\big[\mathbf{F}(\mathbf{y}^{(n+1)}) + \mathbf{F}(\mathbf{y}^{(n)})\big], \tag{24}$$

where Δt is a time step, the superscript (n) denotes the values of vector $\mathbf{y}$ at $t = t_n$. We employ Frechet differentials of the relevant operators to obtain from Eqs. (23), a set of linear ordinary differential equations

$$\mathbf{J}\mathbf{v} \equiv \left[\mathbf{I} - \frac{1}{2}\Delta t\mathbf{F}_y(\mathbf{y}^{(n)})\right]\mathbf{v} = \Delta t\mathbf{F}(\mathbf{y}^{(n)}) \tag{25}$$

in terms of the vector $\mathbf{v}$ that constitutes the increment of the dependent variables between $t = t_n$ and $t = t_{n+1}$

$$\mathbf{v} \equiv \begin{pmatrix} \mathbf{v}_1 \\ \mathbf{v}_2 \end{pmatrix} = \begin{pmatrix} \mathbf{h}^{(n+1)} - \mathbf{h}^{(n)} \\ \mathbf{q}^{(n+1)} - \mathbf{q}^{(n)} \end{pmatrix}. \tag{26}$$

Here $\mathbf{v}_1$, $\mathbf{v}_2$ represent vectors that consist of values of the corresponding functions in the grid points, and $\mathbf{I}$ is a unit matrix.

The matrix $\mathbf{J}$ is a block $2N \times 2N$ matrix, where its upper $N \times 2N$ part arising from Eq. (2) consists of the unit $N \times N$ matrix block on the left and a tridiagonal $N \times N$ matrix block with corner elements due to the periodic boundary conditions on the right. This structure of $\mathbf{J}$ allows to easily express the vector $\mathbf{v}_1$ via $\mathbf{v}_2$ at $t = t_n$ and by substituting it into the lower $N \times 2N$ block of Eq. (25) to finally arrive at

$$\left[\mathbf{I} - \frac{1}{2}\Delta t\mathbf{Q}_q(\mathbf{y}^{(n)})\right]\mathbf{v}_2 + \frac{1}{4}(\Delta t^2)\big[\mathbf{Q}_h(\mathbf{y}^{(n)})\big]\mathbf{v}_{2,x} = \Delta t\mathbf{Q}(\mathbf{y}^{(n)}) - \frac{1}{2}(\Delta t^2)\mathbf{Q}_h(\mathbf{y}^{(n)})\mathbf{q}_x, \tag{27}$$

where $\mathbf{Q}_q$, $\mathbf{Q}_h$ are, respectively, Frechet-differential operators of $\mathbf{Q}$ with respect to q, h calculated at $\mathbf{h} = \mathbf{h}^{(n)}$, $\mathbf{q} = \mathbf{q}^{(n)}$.

Eq. (27) represents a set of N linear ordinary differential equations which, upon spatial discretization using a finite differencing scheme based on a spatially uniform grid of the size Δx and accurate to second order Δx^2, is reduced to a set of linear algebraic equations with a pentadiagonal matrix and triangular corners arising from the periodic boundary conditions. The latter is solved using the modified Thomas algorithm. Evaluation of the Frechet derivatives and spatial discretization are both carried out in the conservative form using linear interpolation for half-nodes, so that in the process of computations the total mass of the film is conserved up to $\mathrm{O}(10^{-12})\%$ of the initial mass, thus verifying Eq. (11). Also, we use Eq. (13) as a criterion for attaining the TW state.

Eqs. (2) and (3) are numerically solved here using the spatially uniform grid of 700 points and a typical initial adaptive time step of order 10^{-3}. During the computation of the spatiotemporal evolution of the film, the time series of the values of h, q and h_t, q_t at $x = 0$ are collected in the time range following the transient period for post-processing. Values of the time derivative q_t are estimated using the backward difference of first order accuracy in Δt. However, the value of h_t is computed directly from Eq. (2), which is accurate to Δt^2, as the dependent variables h, q. These time

series are further used to compute the portrait of the film evolution in the phase plane ($dH - H$), where $H = h/h_N$ and $dH \equiv -q_x/h_N$. We also compute the power spectra of $H(t)$ at $x = 0$ to resolve the degree of nonlinearity of the periodic TW and to characterize thresholds where temporal periodicity is lost.

5. Validation

In this section we investigate the validity of the first-order time-dependent WRIBL equations by comparison of its solutions with: (i) the first- and second-order time-dependent WRIBL [24] and stationary version of WRIBL [20], (ii) stationary [5] and time-dependent [15] DNS, and (iii) experimental data [34]. We recall here that the fixed points of the stationary equations correspond to periodic traveling waves (TW) whose stability is to be determined and that nonstationary wave flows (NSW) are only attainable via solution of the time-dependent equations.

1. *Comparison with WRIBL and BE evolution equation solutions*

(a) Stationary solutions of the evolution equations

A detailed comparison of the stationary WRIBL equations with periodic boundary (or closed flow) conditions was performed by Scheid et al. [20] with the stationary versions of both BE and the time-independent Navier–Stokes equations investigated by Salamon et al. [5] for $W = 1000$.

As noted above, we focus here on the two cases considered in [5,16,17,20], namely: case A in which $W = 1000$, $\varepsilon = 0.04/2\pi$ (equivalent to $\kappa k^2 = 1.6$); and case B in which $W = 1000$, $R = 3.1$ (equivalent to $\kappa = 3374.9$). In both cases we employ periodic boundary conditions (referred to as closed-flow conditions [20]) in the domain $0 \leqslant x \leqslant L$, where $L = h_N \varepsilon^{-1}$. An alternative notation adopted in [20] is $0 \leqslant x \leqslant 2\pi/k$, where k is the fundamental wavenumber, and the relationship between k and ε is given by

$$k = \frac{2\pi\varepsilon}{h_N}. \tag{28}$$

This relationship should assist the reader in comparison between the results presented here and those given in [20]. When compared with the solutions for the BE, Eq. (1), computed in [16] in the domain $0 \leqslant x \leqslant 2\pi$, the latter are rescaled accordingly in the x-direction to fit the domain $0 \leqslant x \leqslant 2\pi$.

Fig. 2 depicts the bifurcation diagram of our solution of Eqs. (2) and (3) for case A. We find that the normalized amplitude for traveling wave solutions grows from the Hopf threshold, $R = 2$, to an abrupt end at $R = 7.6$. We note that the corresponding TW solutions computed by Scheid et al. [20], see their Fig. 2, were found for $2 < R < 9$. They are identical to those in our Fig. 2. However, we were unable to find a continuation of this TW branch ($7.6 < R < 9$), as given in Ref. [20] for traveling wave solutions. We elaborate on this and on additional coexisting and NSW phenomena in the next section.

Fig. 3 presents the bifurcation diagram of our solution for Eqs. (2) and (3) for case B. Here too, our wave amplitudes are identical to those obtained by Scheid et al. [20] for both γ_1- and γ_2-type waves in $0.0035 < \varepsilon < 0.0079$, see their Fig. 3. However, as in case A, we were unable to find the γ_1-type TW for $\varepsilon < 0.004$. We also note that the higher amplitude γ_2-type domain $\varepsilon < 0.004$ incorporate a variety of NSW solutions that we elaborate on in the next section.

(b) Time-dependent evolution equations

A comparison of our results with the time-dependent BE, [17] yields that both TW wave amplitudes of cases A and B are slightly lower than those obtained in BE, see dotted line in Fig. 3. We also compare the spatial evolution of several TW wave forms of case B in Fig. 4 (a), (b), (d), (e). We note that the corresponding solution for BE with $\varepsilon = 0.003394$ is a NSW and is not included in Fig. 4(c).

We solve numerically Eqs. (2) and (3) for the conditions where Ruyer-Quil and Manneville [24] compared their first- and second-order models for closed (periodic boundary) flow conditions with $\kappa = 528.84$ (for alcohol), $\varepsilon = 0.07/(2\pi)$ and $R = 15$. The obtained spatial wave form is depicted in Fig. 5 that accurately reproduces the first-order solution which differs slightly from that obtained from the second-order equation, see their Fig. 5. Note that our non-stationary wave solution resembles the TW-solution [24]. As follows from our numerical solution for Eqs. (2) and (3), each of the humps slightly oscillates in time in the vertical location rendering by this the solution to be NSW.

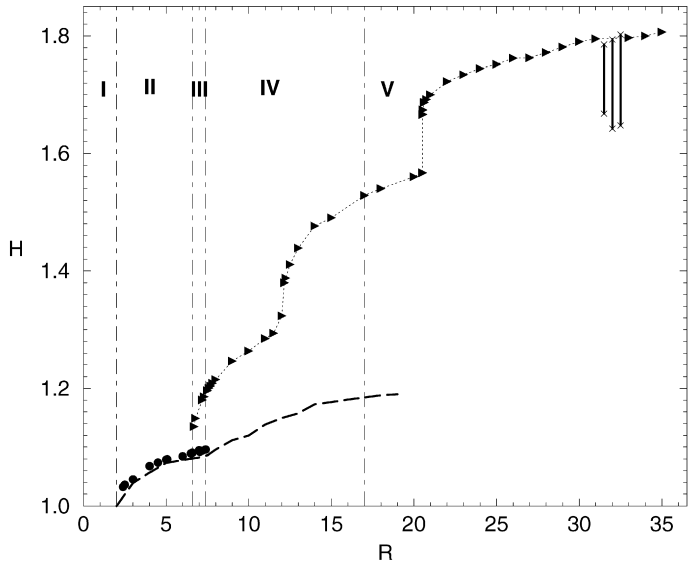

Fig. 2. The bifurcation diagram for case A, as obtained from Eqs. (2) and (3) that shows the value of the normalized wave amplitude H as a function of R. The black circles and triangles represent TW flows of the γ_1- and the γ_2-types, respectively, while the error bars represent the NSW flows showing the variation of H. The dashed curve shows the value of H, as obtained from the direct numerical simulations of TW solutions of the Navier–Stokes equations [5]. The vertical lines demarcate between the various regions: I – the linearly stable domain; II – the domain where only TW flows of the γ_1-type emerge; III – the domain where TW flows of both γ_1- and γ_2-types coexist; IV – the domain where only TW flows of the γ_2-type emerge; V – the domain where the solutions lose the positivity of Q, thus corresponding to flow reversal, see discussion in Section 7.

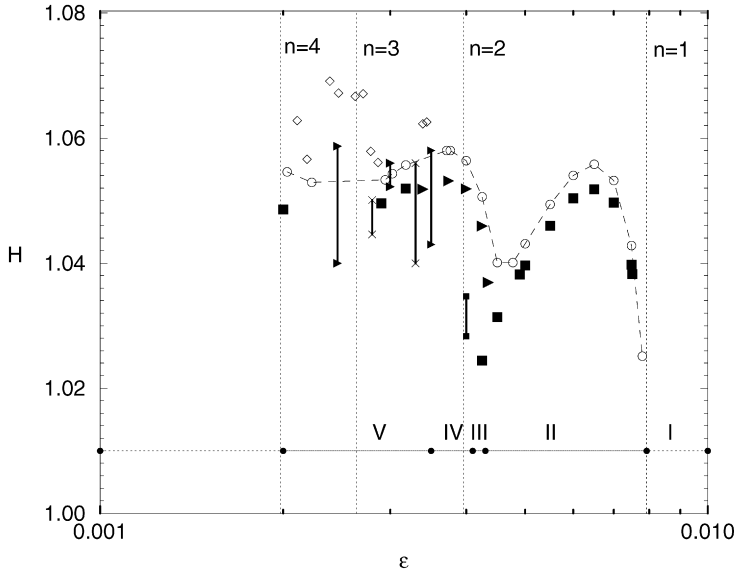

Fig. 3. The bifurcation diagram for case B, as obtained from Eqs. (2) and (3) that shows the normalized wave amplitude H as a function of ε. The black squares and triangles represent TW flows of γ_1- and γ_2-type, respectively, as obtained from Eqs. (2) and (3). The error bars represent the variation of H in the case of the corresponding NSW flows: marked by a black triangle or square when the corresponding NSW is of the γ_2- or γ_1-type, respectively, and marked by $\times$ when it changes its type. White circles (connected to guide the reader's eye) and diamonds represent the TW and NSW solutions, as obtained from the BE, Eq. (1), [17]. The vertical lines $n = 1$ to $n = 4$ represent the linear instability thresholds for the n-th mode, as given by Eq. (20). The black dots indicate the borders between different domains: domain I – the domain of the linear stability of the film; domain II – where only TW solutions for Eqs. (2) and (3) of the γ_1-type exist; domain III – the domain of coexistence between TW solutions of both γ_1- and γ_2-types; domain IV – where TW flows of the γ_2-type coexist with NSW solutions; domain V – where TW flows of the γ_2-type emerge along with replicated TW flows of the γ_1-type and NSW of various kinds.

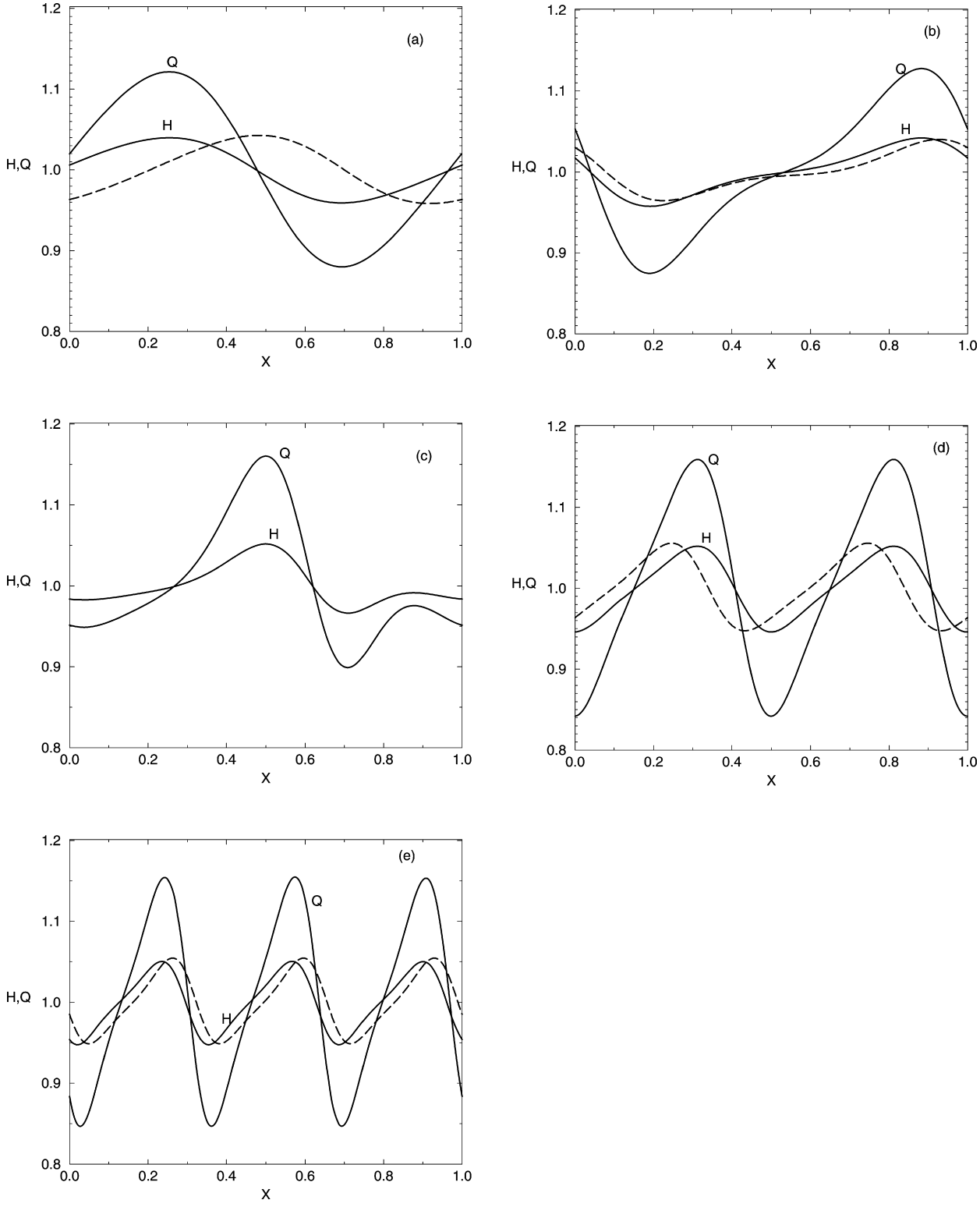

Fig. 4. Sample TW flows $H(X)$ and $Q(X)$, as obtained from Eqs. (2) and (3) in case B (solid curves), and $h(X)$ (broken curves), as obtained from the BE, Eq. (1). (a) $\varepsilon = 0.0075$, (b) $\varepsilon = 0.004775$, (c) $\varepsilon = 0.003394$, (d) $\varepsilon = 0.003183$, (e) $\varepsilon = 0.002$. Note that the corresponding solution for the Benney equation with $\varepsilon = 0.003394$ is NSW [16] and therefore is not included in (c).

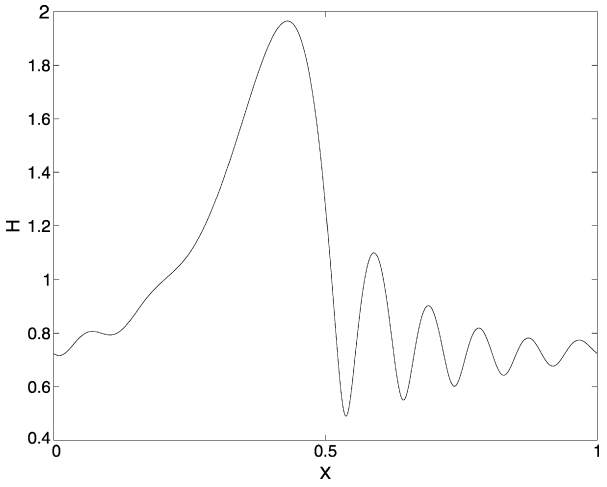

Fig. 5. The wave profile for an alcohol film. This solution represents a non-stationary solution for Eqs. (2) and (3) with $R = 15$, $\kappa = 528.84$ and $\varepsilon = 0.072/2\pi$. It only slightly deviates from the second-order solution in Fig. 5, [24].

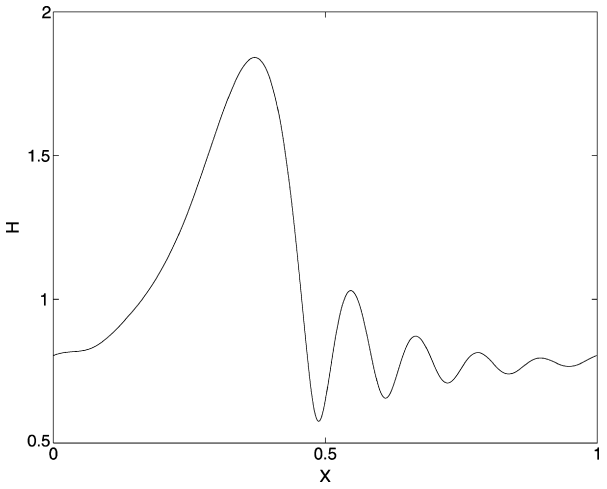

Fig. 6. The wave profile for an alcohol film obtained from Eqs. (2) and (3) with $R = 9.1$, $\kappa = 528.84$ and $\varepsilon = 0.0111$. This solution is a traveling wave.

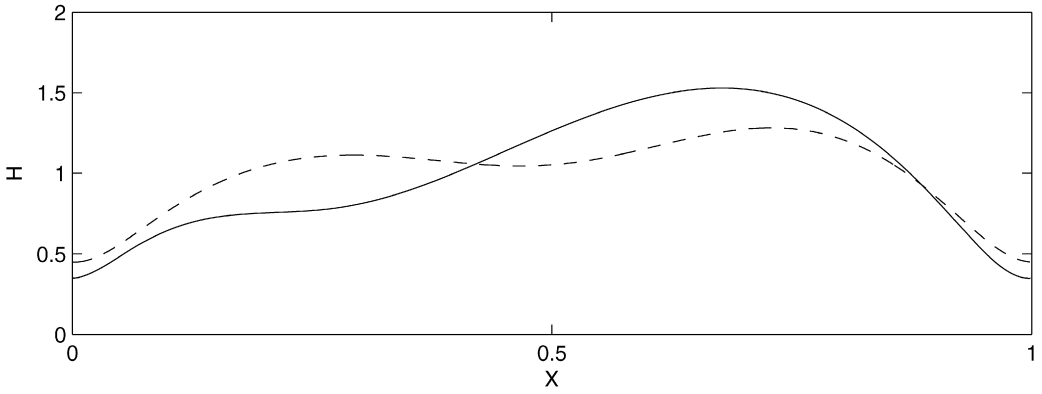

Fig. 7. The wave profile for a water film. This solution represents a non-stationary wave obtained from Eqs. (2) and (3) with $R = 30.1$, $\kappa = 3379$ and $\varepsilon = 0.0222$. The solid and dashed curves correspond to the solutions with the largest and smallest amplitudes, respectively.

2. *Comparison with solutions of the Navier–Stokes equations*

Salamon et al. [5] validated their stationary solutions for conditions of experiments [34] for both alcohol ($\kappa = 528.84$) and water ($\kappa = 3379$). However, their results only qualitatively reproduced the shadow diagrams of the experiments as shown in their Figs. 9 and 10. Ramaswamy et al. [15] performed time-dependent numerical simulations and we can quantitatively compare our results with theirs.

We first depict in Fig. 6 the traveling wave solution obtained for the conditions of the experiment [34] with alcohol films. We note that our solution is almost identical to that of [15], see their Fig. 2b. Our solution for conditions of the experiment with water [34] is shown in Fig. 7. We obtain an NSW depicted by two representative snapshots, which is almost identical to that of [15], see their Fig. 4b. We note that Salamon et al. [5] who employed a stationary version of the equation could only obtain a TW and were unable to test the emergence of NSW. Gao et al. [7] also reported the emergence of a NSW solution obtained from the Navier–Stokes equations. However, the amplitude of their wave (see Fig. 5, [7]) is much lower than in the corresponding solution shown here in Fig. 7 and Ramaswamy et al. [15].

Following Ref. [15] we simulate conditions where $\kappa = 300$ and $R = 12.5$, and where we vary the value of $\varepsilon = 0.07$ to correspond to the three spatial TW forms in Fig. 8. We note that the first two solutions with $k = 0.3$ and $k = 0.15$, are identical to those obtained by direct numerical simulations [15], as they correspond to a single- and three-mode

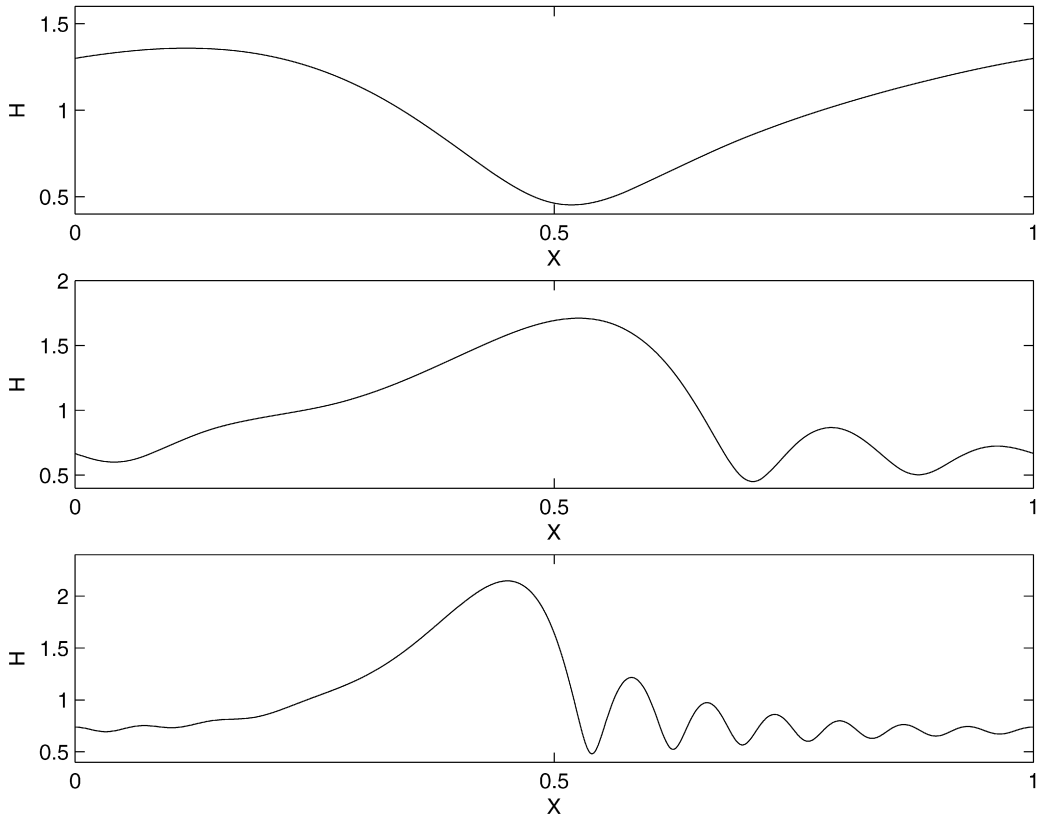

Fig. 8. The wave profiles obtained from Eqs. (2) and (3) with $R = 12.5$, $\kappa = 300$. The solutions presented are TW and correspond to $\varepsilon = 0.00477$, 0.02387 and $\varepsilon = 0.01194$ from the top to the bottom, respectively.

solutions. The TW obtained with a growing nonlinearity for $k = 0.075$, is slightly lower than that obtained [18] in their Fig. 7f.

Nosoko and Miyara [9] performed numerical solution of Navier–Stokes equations for falling vertical water films. In Fig. 9, we present several solutions of Eqs. (2) and (3) corresponding to the numerical solutions of Nosoko and Miyara [9] for $R = 24.15$ and $\kappa = 3375.9$ (e.g., $Re = 16.1$ in their notation) presented there in Figs. 2a–2d, and for $R = 77.25$ (e.g., $Re = 51.5$ in their notation) presented there in Fig. 1e. The respective values of the periodicity are determined directly from the patterns computed in [9]. The solutions presented in Fig. 9 represent a slightly oscillating NSW in (a), TW of the γ_2-type in (b) and (d), and TW of the γ_1-type in (c) and (e). The topological similarity between the solutions of Eqs. (2) and (3) and the respective solutions displayed in Figs. 2a–2d and Fig. 1e of [9] is evident. A comparison between the amplitudes presented in (a) reveals a fit of 9%: the amplitude of the solution obtained by Nosoko and Miyara [9] in their Fig. 2a is 0.214 mm, whereas the amplitude of our NSW solution recalculated in *mm*, varies between 0.213 mm and 0.236 mm. A similar comparison between the amplitudes for the solutions in (b) and (d) reveals a fit of 17%: 0.186 mm in our solution versus 0.154 mm in [9] in the former, and 0.153 mm in our solution vs. 0.128 mm in [9] in the latter. A comparison between the amplitudes of the solutions in (c) and (e) with those of [9] in their Fig. 2c and 1e, respectively, shows an excellent agreement of less than 3% in the former: 0.187 mm in our solution vs. 0.182 mm in [9], and less than 6% in the latter: 0.234 mm in our solution vs. 0.249 mm in [9].

3. *Comparison with experiments*

In this section we carry out a comparison of the solutions for Eqs. (2) and (3) subjected to the periodic boundary conditions and the experimental observations found in the literature.

As described above, our solutions for conditions of the alcohol and water experiments [34] are almost identical to those obtained in [5,15]. Thus, they qualitatively match the shadow graphs presented by Kapitza and Kapitza [34]. We

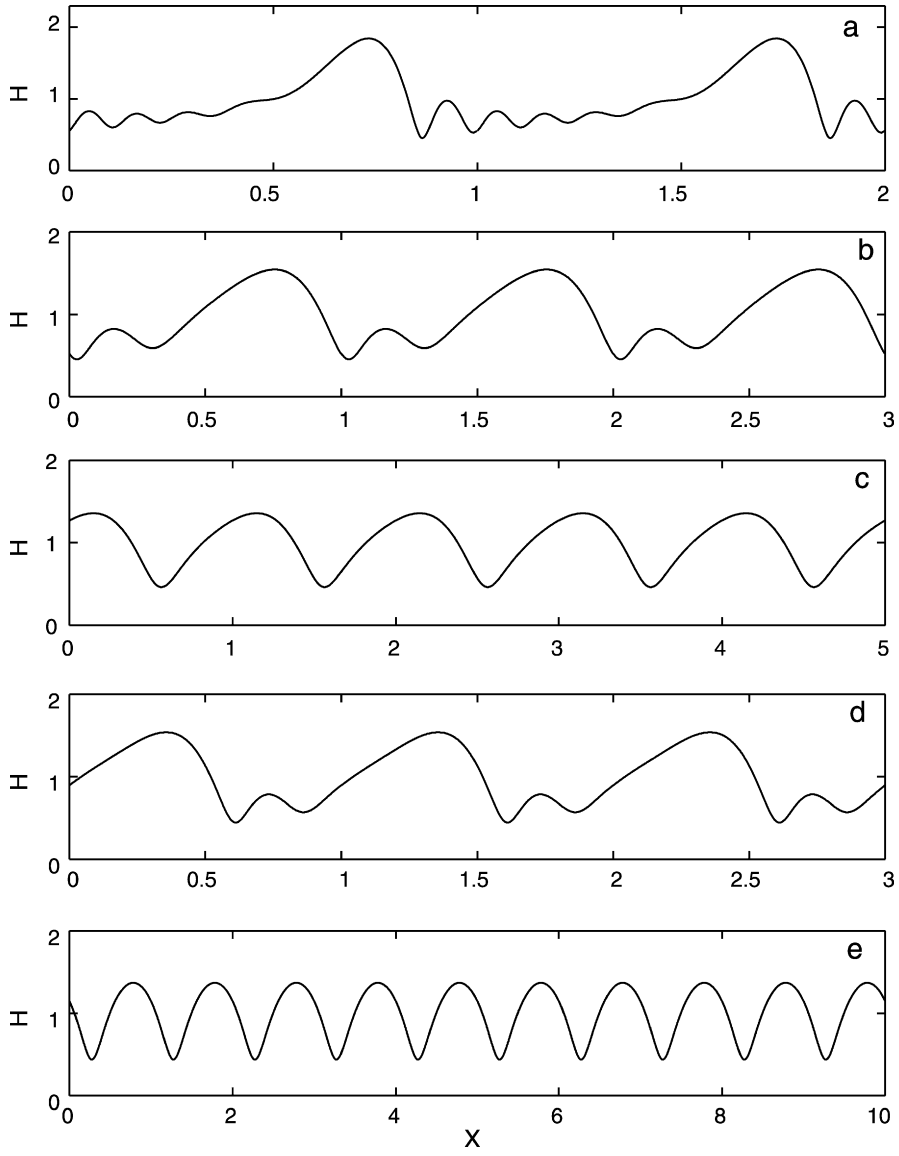

Fig. 9. The wave profiles obtained from Eqs. (2) and (3) with $\kappa = 3375.9$ and (a)–(d) $R = 24.15$; (e) $R = 77.25$. The solution presented in (a) is a slightly oscillating NSW, whereas those presented in (b)–(e) are TW. The solutions presented in (a), (b) and (d) are of the γ_2-type, whereas those in (c) and (e) are TW of the γ_1-type.

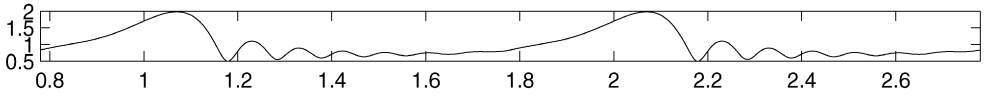

Fig. 10. The wave profile obtained for an alcohol film from Eqs. (2) and (3) with $R = 9.1$, $\kappa = 528.84$ and $\varepsilon = 0.01114$. This solution represents a traveling wave.

combine several TW and NSW spatial wave forms together for alcohol and water, respectively, in Figs. 10 and 11, so that they are in the same form, as the original results [34].

The experiments of Alekseenko et al. [36] show that in the observations summarized in their Figs. 8 and 9, the amplitude of the interfacial wave saturates at the distance of $220d$ and becomes almost constant downstream for a significant stretch. We now solve Eqs. (2) and (3) in the periodic domain whose length is determined from the

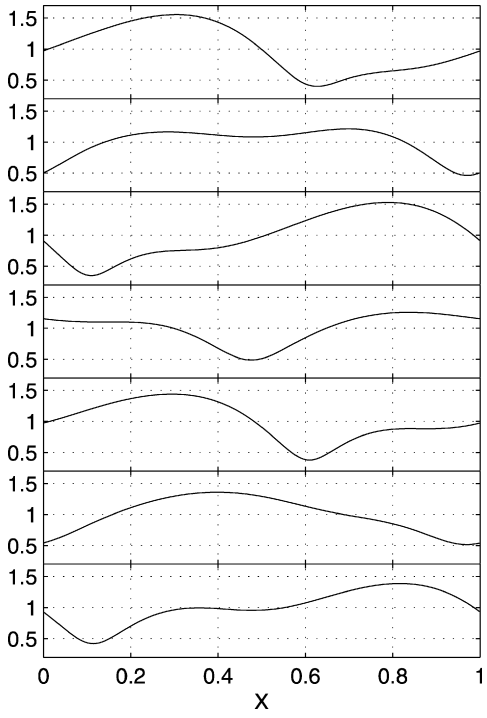

Fig. 11. The wave profile obtained for a water film from Eqs. (2) and (3) with $R = 30.1$, $\kappa = 3379$ and $\varepsilon = 0.02228$. This solution represents a non-stationary wave.

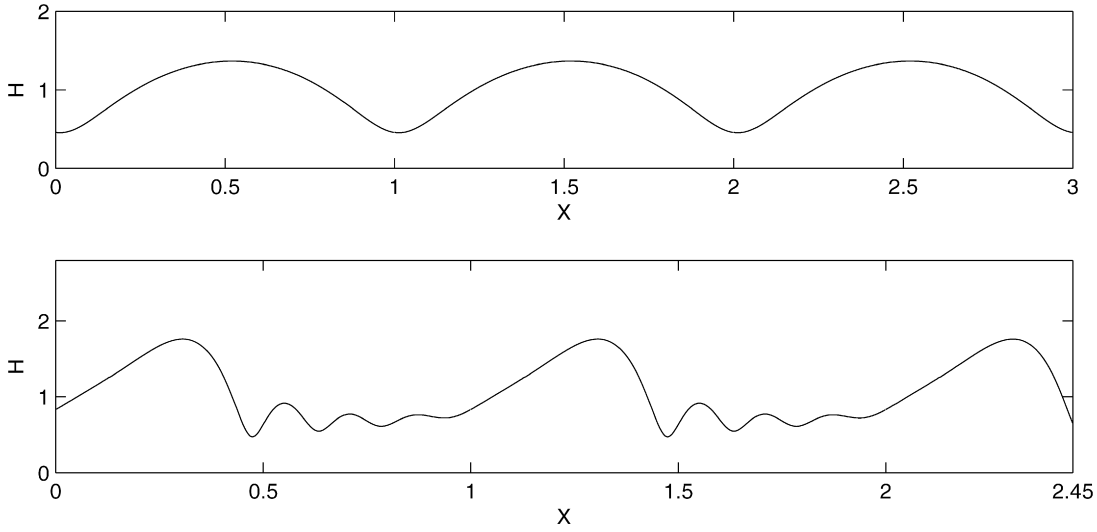

Fig. 12. (upper panel) TW solution of the γ_1-type obtained from Eqs. (2) and (3) with $\kappa = 905.2$, $R = 54.3$ and $\varepsilon = 0.1063$ corresponding to $x/d = 240$ in Fig. 9 of Alekseenko et al. [36]; (lower panel) TW solution of the γ_2-type obtained from Eqs. (2) and (3) with $\kappa = 905.2$, $R = 22.75$ and $\varepsilon = 0.0179$ corresponding to $x/d = 240$ in Fig. 7e of Alekseenko et al. [36].

experimental pattern wavenumber $k \approx 0.14$ specified in their Fig. 9 at $a/h_0 \approx 1$ for $R = 54.3$. Here $\kappa = 905.2$ and $\varepsilon = 0.1063$. Note the difference in the definition of the Reynolds number R here and Re in [36], $R = 3Re/2$. The shape of the γ_1-type TW obtained here from Eqs. (2) and (3) and displayed in the upper panel of Fig. 12, is fairly sinusoidal and its normalized wave height, $(h_{\max} - h_{\min})/h_N$, is 0.91 which is 9% lower than the experimental measurement in Fig. 8 [36]. We note that the parameter set of this experiment corresponds to that of one linearly unstable mode,

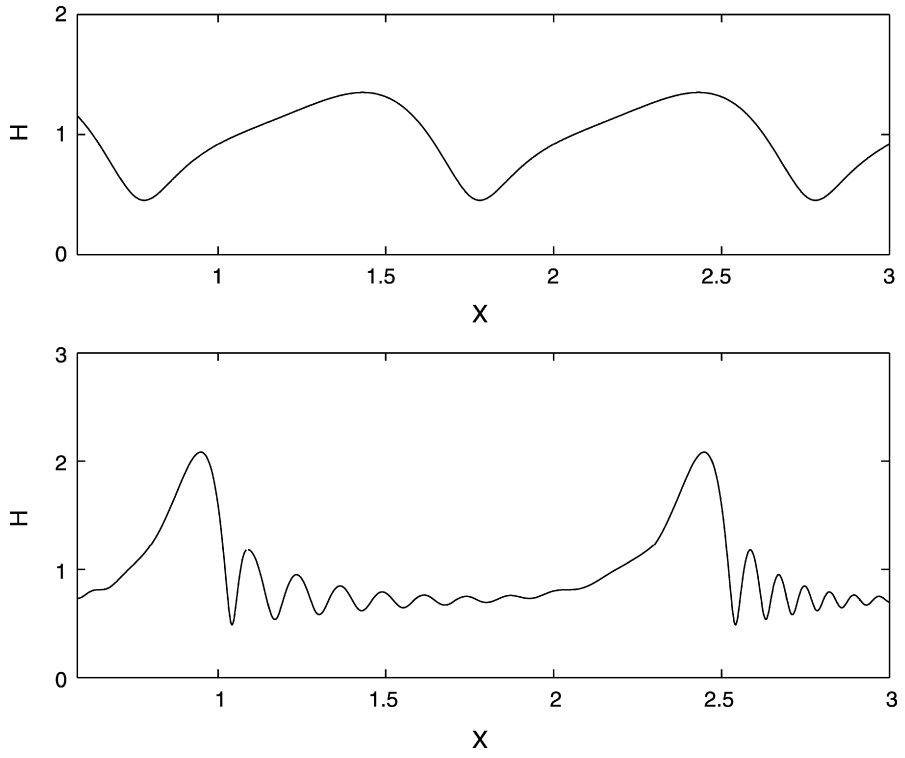

Fig. 13. Profiles of interfacial waves, as obtained from Eqs. (2) and (3) to compare with the experiments of Alekseenko et al. [37] shown in Fig. 8-26 there. In both cases $\kappa = 193.5$ and $R = 10.8$ which is equivalent to their $Re = 7.2$. Upper panel – $\varepsilon = 0.0449$; lower panel – $\varepsilon = 0.0141$. The solutions presented here are both very slightly varying NSW.

$\varepsilon_2 < \varepsilon < \varepsilon_1$, as computed by Eq. (20). The normalized wave celerity, as obtained from our numerical solution is 2.19, is 9% larger than in the experiments indicated in Fig. 9 [36].

The lower panel of Fig. 12 presents the solution for Eqs. (2) and (3) in the domain $0 \leqslant X \leqslant 1$with the parameters obtained from the experimental observations given in Fig. 7e of Alekseenko et al. [36] which represents the wave evolution far from the inception domain, $x/d = 240$. The presented experimental data in Fig. 7e, [36] is almost periodic in space and therefore may serve for a comparison with the periodic solutions of Eqs. (2) and (3). The value of $\varepsilon = 0.0179$ was determined from the wave speed $c = 280$ mm/s given in [36] and the rest of parameters are $\kappa = 905.2$, $R = 22.75$. The wave regime shown in the lower panel of Fig. 12 represents a slightly varying NSW of the γ_2-type which consists of one large hump and three smaller ripples in one spatial period and whose amplitude is 35% larger than in the experiment. This discrepancy can be associated with the large number of unstable modes, $\varepsilon_5 < \varepsilon < \varepsilon_4$, as computed from Eq. (20).

Fig. 13 displays the solutions for Eqs. (2) and (3) obtained for the parameters corresponding to the experimental conditions given in [37], see Fig. 8.26 there, $\kappa = 193.5$ and $R = 10.8$. The periodic boundary conditions corresponding to the wavelength λ specified in the experiments were imposed in our computation. The solutions shown in the upper and lower panels correspond to $\varepsilon = 0.0449$ and $\varepsilon = 0.0141$, respectively, and are both very slightly varying NSW. The topology of the experimental wave profiles and their types, of γ_1 and γ_2, are reproduced very well. The normalized wave heights of our solutions are somewhat larger than in the experiments: 0.89 in our numerical solution is 21% larger than in the experiment in the upper panel, and 1.59 is 30% larger than in the experiments in the lower panel. We note that the difference in wave heights may be associated with the large number of unstable modes $\varepsilon_7 < \varepsilon < \varepsilon_6$. Furthermore, we note that the Kapitza number for this experiment may not be sufficiently large, as required by the model [24,25]. Larger values of the Kapitza number would introduce an additional suppression of the unstable modes and lead to reduction of the solutions amplitude.

Fig. 14 presents the solutions for Eqs. (2) and (3) obtained for the parameters corresponding to the experimental conditions given by Alekseenko et al. [36,37] presented there in Fig. 13 and Fig. 8.25, respectively, for $\kappa = 193.5$

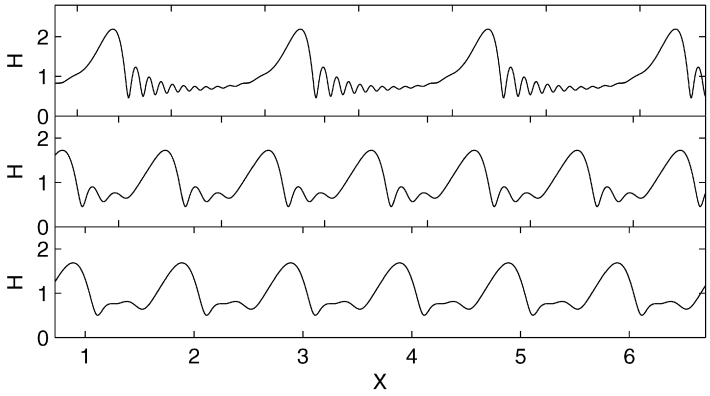

Fig. 14. Profiles of interfacial waves, as obtained from Eqs. (2) and (3) to compare with the experiments of Alekseenko et al. [36,37] shown there in Figs. 13 and 8-25, respectively. In all the three cases $\kappa = 193.5$ and $R = 12.1$ which is equivalent to their $Re = 8.05$. Upper panel – $\varepsilon = 0.0132$; middle panel – $\varepsilon = 0.0280$; lower panel – $\varepsilon = 0.0331$. The solution presented in the upper panel is TW, while the others are NSW.

and $R = 12.1$. The shapes of the interfacial waves shown there, represent approximately spatially periodic waves characterized by the authors as "stationary two-dimensional waves". In our computations, the solution shown in the upper panel corresponds to $\varepsilon_8 < \varepsilon < \varepsilon_7$ and is indeed a TW, while the two others are NSW both corresponding to $\varepsilon_4 < \varepsilon < \varepsilon_3$. From the comparison between Fig. 14 and the experimental figures one finds that the topology of the interfacial waves in the two upper panels agree quite well if the small ripples in front of the large humps are consolidated into larger entities. On the other hand, the solution shown in the lower panel is different from the experimental observation subjected to high-frequency perturbations that significantly reduces the amplitude of the interfacial wave and renders it nearly sinusoidal. For some reason, the discrepancy between theory and experiments here is larger than in other cases. Similar to the solutions presented in Fig. 13, the difference in the normalized wave heights of the numerical solutions and the experimental observations ranges between 35% and 40%, which can also be explained by the fact that the Kapitza number is not sufficiently large. We note that according to Alekseenko et al. [36], the high- frequency upstream disturbance strongly affects the wave pattern diminishing its amplitude and making it almost sinusoidal. Thus, the pattern depicted in the lower panel of Fig. 14 bears the highest degree of discrepancy, i.e. the wave height and its type. We have also found that the value of the wave celerity in the TW case shown in the upper panel is 15% larger than in the experimental observation.

6. Numerical investigation

It is readily seen that Eqs. (2) and (3) are not invariant under the transformation $h \to h_N - h$, $q \to q_N - q$, hence their solutions are not expected to be symmetric with respect to the equilibrium state, $h = h_N$, $q = q_N$. Thus, in general $h_{\max} - h_N \neq h_N - h_{\min}$. To characterize the asymmetric solutions for Eqs. (2) and (3) we use here the classification made by Chang [28] for the waves emerging in falling liquid films: (i) the γ_1-family whose representatives satisfy the condition $h_{\max} - h_N < h_N - h_{\min}$, i.e., depression or "hole" waves, and (ii) the γ_2-family whose representatives satisfy the condition $h_{\max} - h_N > h_N - h_{\min}$, i.e. elevation or "hump" waves.

A. *Case A*

1. Bifurcation structure

As noted above, the stability threshold of the system in case A is given by $R = R_1 = 2$. To investigate the film dynamics in the unstable domain we solve Eqs. (2) and (3) numerically in the range of $2 < R \leqslant 35$ and the results are shown hereafter. Fig. 2 presents the normalized amplitude $H = h_{\max}/h_N$ of the film thickness given by the solution for Eqs. (2) and (3) reached after the transient period as a function of R. In this figure the value of H is indicated by an appropriate point when the corresponding solution is a traveling wave (TW), and by a bar showing the variation range of H in the large-time limit when the corresponding solution is a non-stationary wave (NSW). It is found that the solutions in the domain $2 < R < 6.6$ are TW of the γ_1-family, represented by the solution for $R = 5$ shown in Figs. 15(a), 16(a) and 17(a), where $X = \varepsilon x/h_N$ and $Q = q/q_N$. In the range of $6.7 \leqslant R \leqslant 7.6$, we find coexisting TW of both γ_1- and γ_2-families, as shown in Fig. 18. The abrupt termination of the γ_2-branch at $R \approx 6.7$ suggests

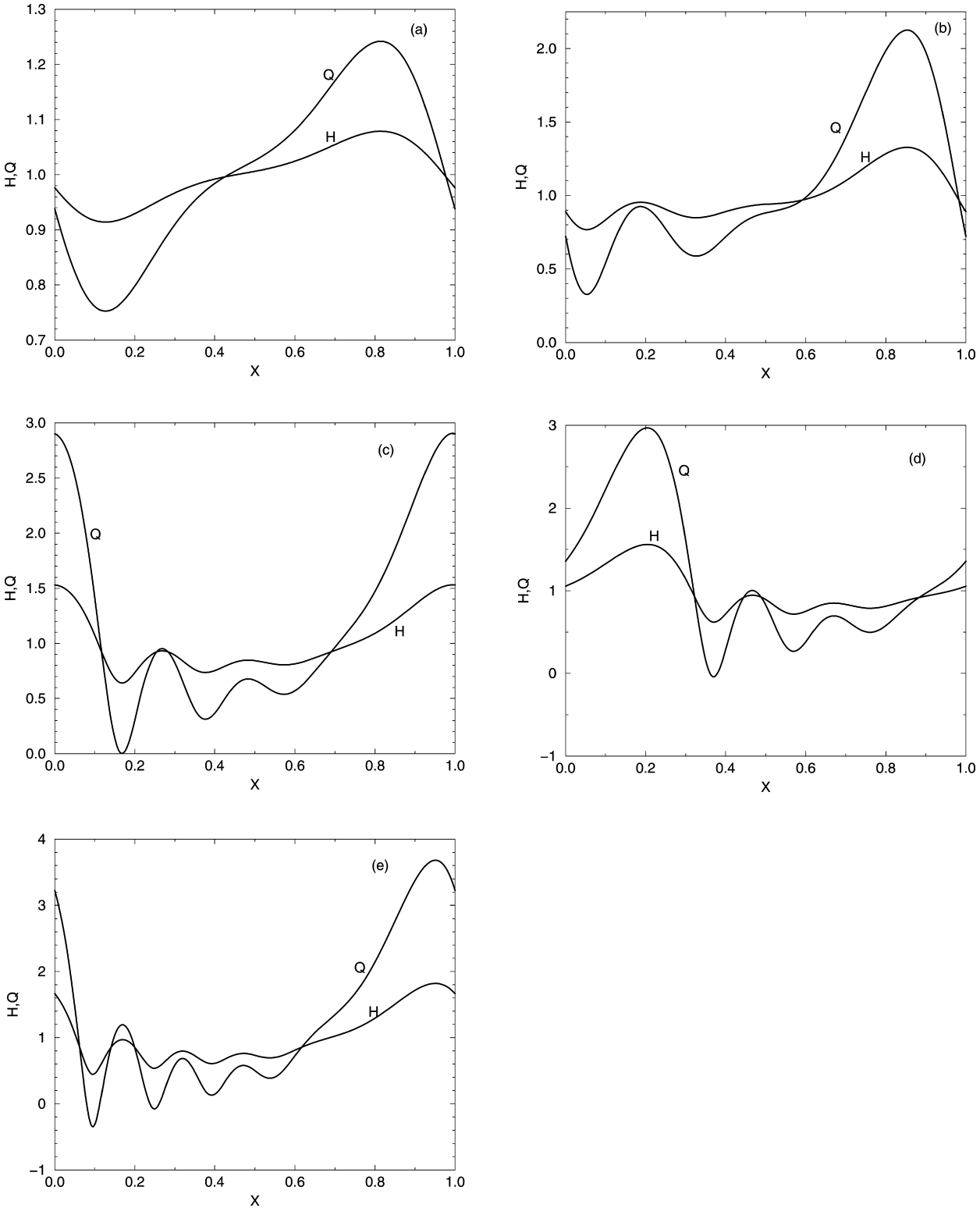

Fig. 15. Sample TW flows presented by $H(X)$ and $Q(X)$ with $X = \varepsilon x/h_N$, as obtained from Eqs. (2) and (3) in case A: $W = 1000$, $\varepsilon = 0.04/2\pi$. (a) $R = 5$, (b) $R = 12$, (c) $R = 17$, (d) $R = 20$, (e) $R = 35$.

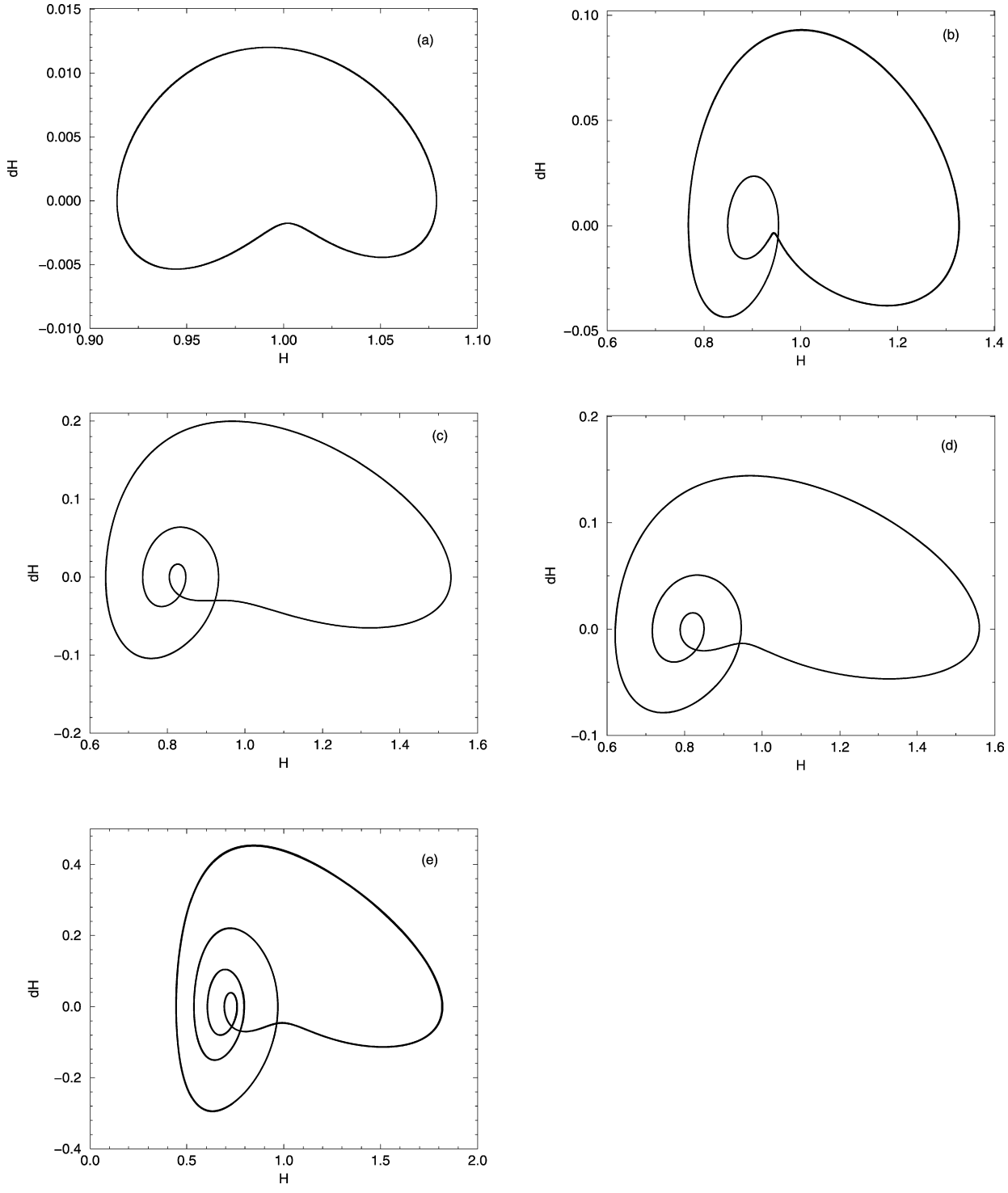

Fig. 16. Phase plane portraits for the TW flows shown in Fig. 14. (a) $R = 5$, $2500 \leqslant t \leqslant 3000$; (b) $R = 12$, $2500 \leqslant t \leqslant 3000$; (c) $R = 17$, $2500 \leqslant t \leqslant 3000$; (d) $R = 20$, $4000 \leqslant t \leqslant 5000$; (e) $R = 35$, $2500 \leqslant t \leqslant 3000$.

the existence of secondary bifurcation at $R = \widehat{R}$, and due to this, the existence of another, unstable TW branch in the interval $6.6 < R < \widehat{R}$. This unstable branch cannot be recovered by numerical solution of the pertinent partial

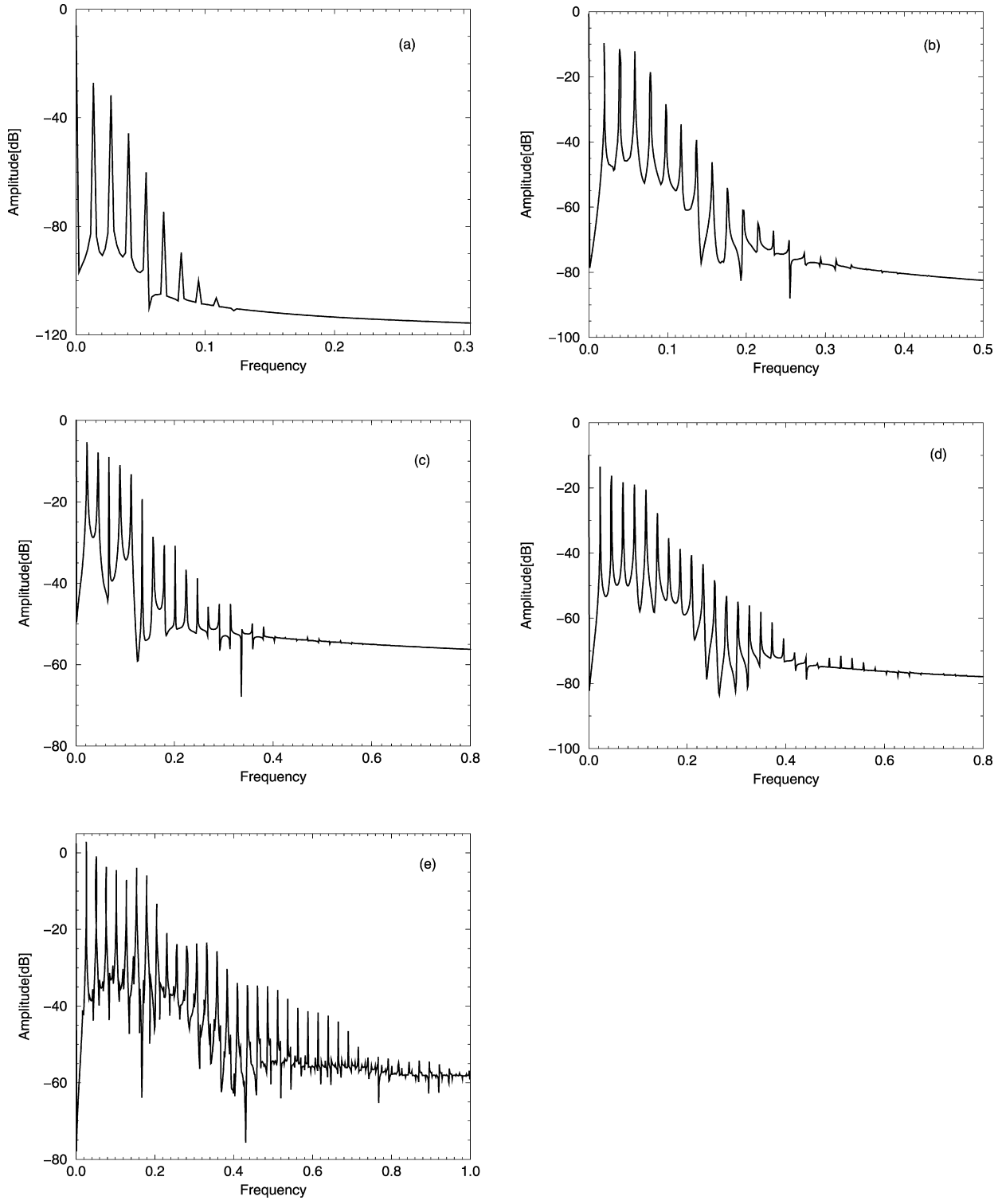

Fig. 17. Power spectra of the temporal evolution for the TW flows shown in Fig. 14 in the time ranges given in Fig. 16.

differential equations. In the domains $7.7 \leqslant R \leqslant 31$ and $33 \leqslant R \leqslant 35$, TW of the γ_2-family are only present. We also find that solutions of Eqs. (2) and (3) within the interval $31.5 \leqslant R \leqslant 32.5$ are NSW.

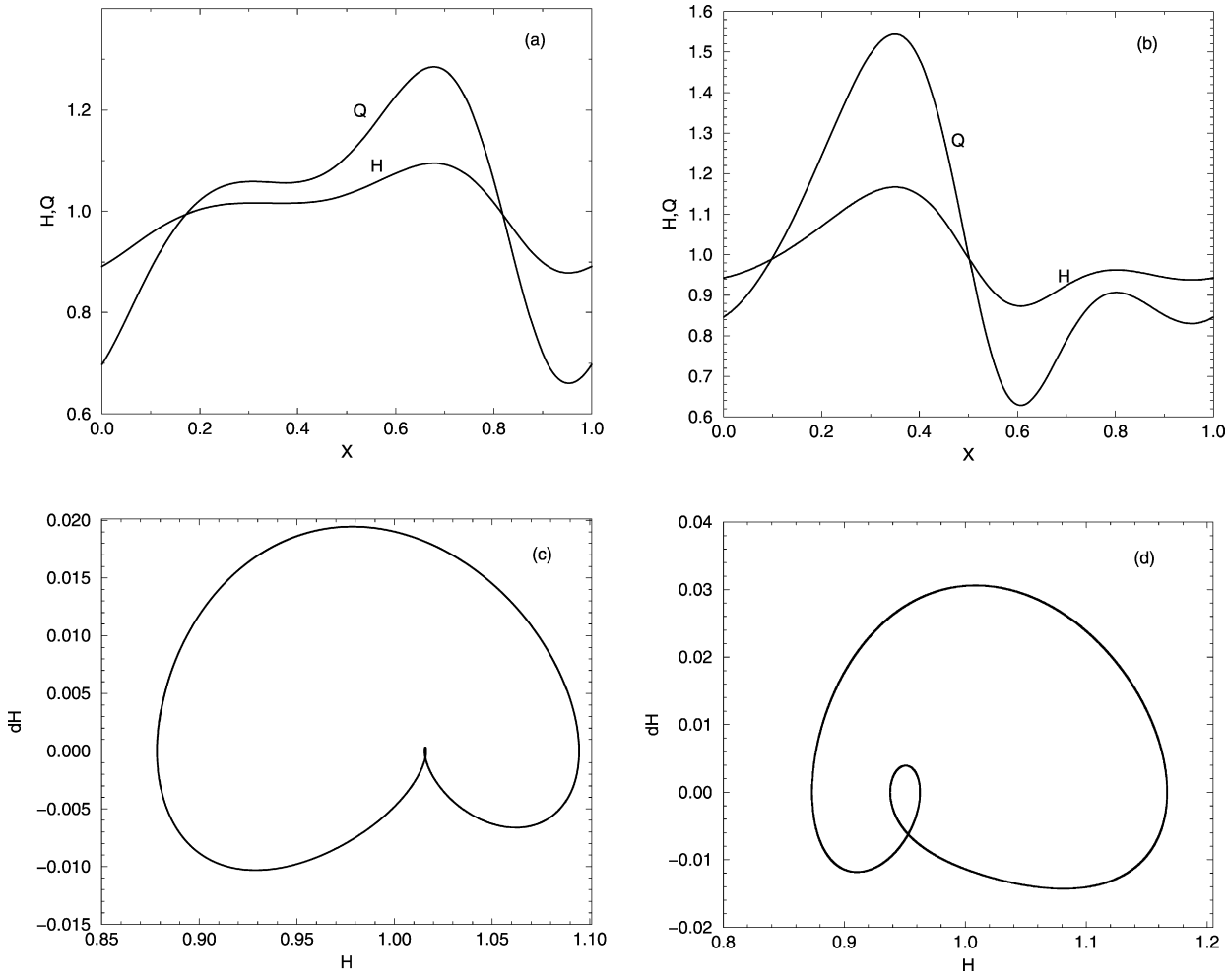

Fig. 18. Coexisting TW flows, as obtained from Eqs. (2) and (3) in case A for $R = 7$ ($h_N = 2.410$). (a), (c): the γ_1-wave; (b), (d): the γ_2-wave. (a), (b): the corresponding solutions $H(X)$ and $Q(X)$. (c), (d): the corresponding phase plane portraits, for the γ_1- and γ_2- waves $9500 \leqslant t \leqslant 10000$ and $2500 \leqslant t \leqslant 3000$, respectively.

2. Traveling wave solutions

A few of the representatives of the TW solutions are shown in Figs. 15, 16 and 17 for $R = 5, 12, 17, 20$ and $R = 35$, respectively. The results of our computations show that in the vicinity of $R = R_n$, the number of wave humps increases by one complying with the results of the linear theory. However, we have not found replicated waves defined by TW flows consisting of two or more identical humps, and all multi-humped flows we have obtained, consist of one major wave and one or more smaller ones.

It is important to emphasize that the γ_1-type TW computed here in the range of $R_1 \leqslant R \leqslant 7.4$, are very similar in their amplitude and topology to those obtained by Scheid et al. [20] using AUTO software designed for search for TW solutions. Their amplitudes are also in a very good agreement with the TW obtained by Salamon et al. [5], who unfortunately did not specify the type (γ_1 or γ_2) of the waves in the case at hand. It is also important to note that the first-order Benney equation, Eq. (1), possesses bounded solutions in case A for $R < 7.2$, [16], and all of them are TW of the γ_2-family. Their amplitudes also agree well with the results of direct numerical simulations of the Navier–Stokes equations carried out by Salamon et al. [5], as shown in [16]. Eqs. (2) and (3) display a "jump" from the γ_1-wave branch to the γ_2-branch of solutions. Scheid et al. [20] investigated TW solutions for Eqs. (2), (3) and found that the γ_1-branch bifurcating at $R = R_1$ exists until $R = 9$ (their $Re = 6$) and extends even further into the domain of higher R, as communicated to us by Benoit Scheid. We have attempted to follow our γ_1-branch from $R = 7.4$ and on, using both the "standard" initial condition, the continuation method starting from the solutions [20] of the γ_1-type and

also from the solutions of our γ_1-branch at $R \approx 7.4$ as initial conditions. However, the ensuing evolution has resulted in the emergence of the corresponding TW solutions on the γ_2-branch. Therefore, our conclusion is that the γ_1- branch becomes unstable for $R > 7.4$.

As follows from our computations, all solutions of Eqs. (2) and (3) in case A are TW in the range $2 < R \leqslant 31$ and $33 \leqslant R \leqslant 35$, with a general trend of increasing the peak-to-peak sizes of both H and Q with increase of R, as shown in Fig. 15. Along with increase of the peak-to-peak size of Q, there are both increase of $Q_{\max}$ and decrease of $Q_{\min}$, so that at $R \approx 17$, the value of $Q_{\min}$ approaches zero, as shown in Fig. 15(c), and for $R > 17$, $Q_{\min}$ becomes negative and remains negative in a certain range $X_1(t; R) < X < X_2(t; R)$ below the depression of the film interface. This range expands with increase of R, see Fig. 15(c)–(e). This issue is further addressed in Section 7.

Figs. 16 and 17 show the temporal evolution of the value $H(X = 0, t)$ for the TW solutions shown in Fig. 15, in the phase plane $H - dH$ and via the power spectra, respectively. The results clearly indicate the time-periodic character of the film dynamics, as represented by these solutions for Eqs. (2) and (3). We note that, as expected for an increased nonlinearity for growing R, the complexity of the γ_2-type TW increases, as depicted by the increasing number of humps in Fig. 15(e), 16(e) and denser spectra, Fig. 17(e).

3. Non-stationary wave solutions

As noted above, Eqs. (2) and (3) admit along with TW solutions also NSW solutions. In case A, the NSW flows are obtained in the range of relatively large Reynolds numbers, $31.5 \leqslant R \leqslant 32.5$. These flows belong in the domain, where Eqs. (2) and (3) lose the positivity of Q, see Section 7. One of them, $R = 32$, is shown by the time evolution of $H(X = 0, t)$ in both phase plane and temporal power spectrum in Fig. 19. The dense phase plane, Fig. 19(a), and an irregular spectrum, Fig. 19(b), suggest that the evolution of this wave is aperiodic. The neighboring solutions for $R = 31.5$ and $R = 32.5$ are very similar to this. The contents of Fig. 19(c) will be discussed in Section 7.

4. Coexisting solutions

As noted above, a domain of coexisting γ_1- and γ_2-TW was found to be $6.7 \leqslant R \leqslant 7.6$, see region III in Fig. 2. It is important to note that the solutions displayed in Figs. 2 and 15 were obtained using the "standard" initial condition and the method of continuation from the solutions obtained for adjacent values of R. However, the coexisting γ_2-branch whose emergence is noted above, see Section 6(A1), was obtained in the range $6.7 \leqslant R \leqslant 7.6$ solely by initiating the continuation from TW at $R = 7$. Fig. 18 displays the coexisting TW solutions of both γ_1- and γ_2-types for $R = 7$, as functions $H(X)$ and $Q(X)$, and their temporal evolution is shown in the phase plane. While the amplitude of the γ_2-wave is larger than that of the γ_1-wave, their spatial structures are similar.

We note here that this coexistence was also noticed by Scheid et al. [20] who searched for TW solutions, see their Fig. 3. However, their analysis dealt with the search of TW solutions and did not investigate stability of the coexisting solutions. Thus, our analysis reveals that the transition from region II to region III in Fig. 3 is indeed a pitchfork bifurcation after which two stable attractors are born, Fig. 18. Note that these attractors are separated by an unstable solution. Thus, we conclude that the middle branch in Fig. 3a, [20] is an unstable TW of γ_1-type.

B. *Case B*

1. Bifurcation structure

Fig. 3 displays the bifurcation diagram for case B in the plane $\varepsilon - H$. We have divided the investigated domain $0.002 \leqslant \varepsilon \leqslant \varepsilon_1$ into several regions where solutions of Eqs. (2) and (3) possess different properties. In region I ($\varepsilon \geqslant \varepsilon_1$), the base Nusselt state $h = h_N$, $q = q_N$ is linearly stable. In region II ($0.0045 \leqslant \varepsilon \leqslant \varepsilon_1$), Eqs. (2) and (3) display only TW solutions of the γ_1-type shown by the black squares. This γ_1-branch continues a little further up to the point at $\varepsilon = 0.00425$ located in the vicinity of the intersection point (IP) found by Scheid et al. [20], see their Fig. 3. The amplitude H of these solutions is in a very good agreement with the results obtained by Scheid et al. [20] for TW solutions. In the narrow region III located in the neighborhood of IP the coexistence between TW flows of both γ_1- and γ_2-families, shown by black triangles, takes place. This coexistence is similar to that obtained in case A, see Section 6(A4) and Fig. 18, and we notice, similarly to case A, that the emergence of the γ_2-type TW is due to a secondary bifurcation, as in Scheid et al. [20]. In region IV the γ_2-type TW flow found within region III at $\varepsilon = 0.00435$ is followed by the γ_2-branch indicated by the black triangles, up to $\varepsilon = 0.00374$. The emergence of the TW branch of γ_2-type following the domain of coexistence of both types of TW is similar to case A. However, the differences between these two cases are found to the left of region IV. Region V contains interdispersed solutions of the γ_2-type both TW and NSW solutions (shown by error bars with triangles), as well as NSW solutions switching between the γ_1- and the γ_2-types (shown by error bars with $\times$), and also TW flows of the γ_1-family (shown by black squares). The latter represent replication of uni-humped TW solutions of Eqs. (2) and (3) located along the ascending branch of TW

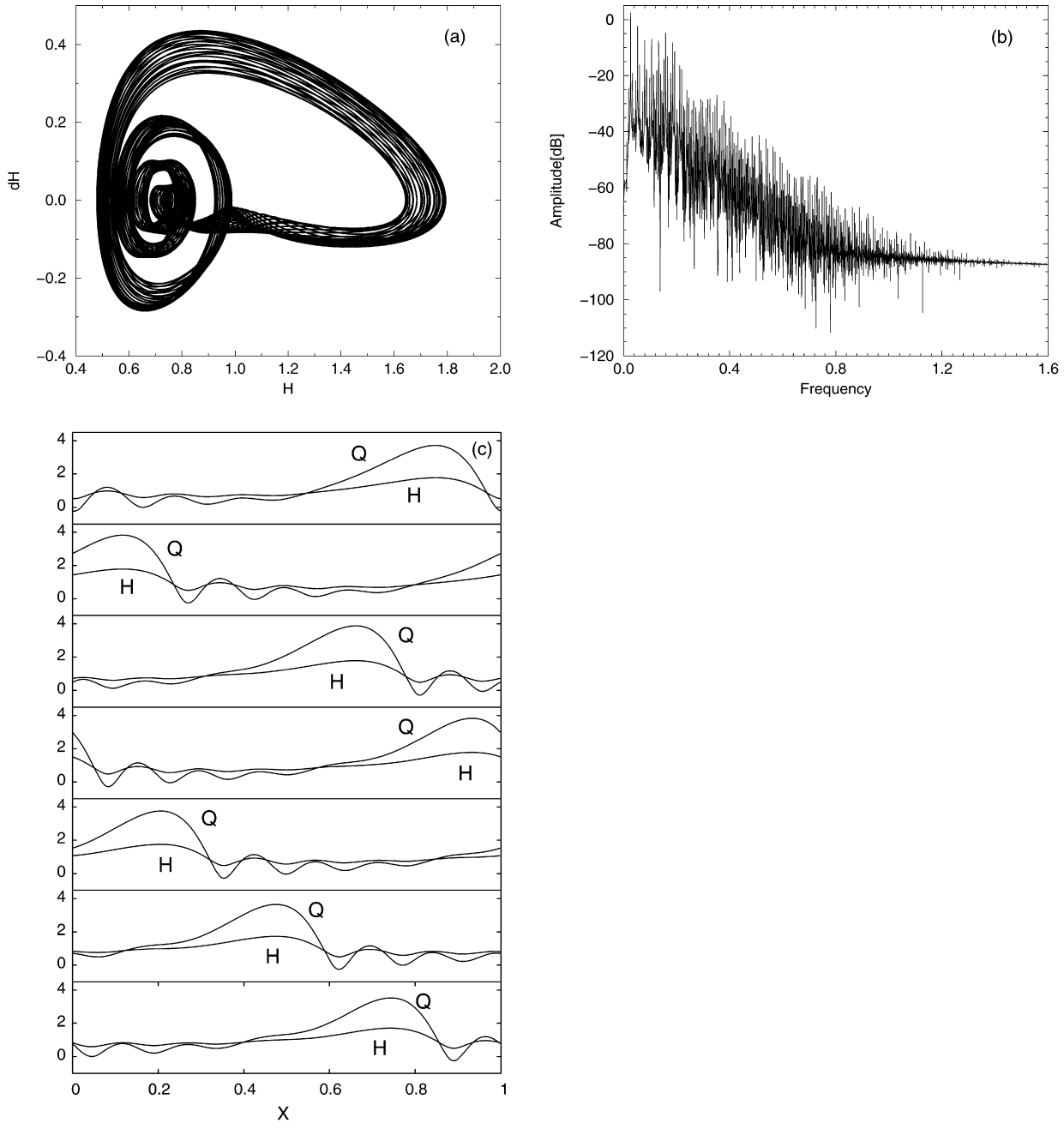

Fig. 19. (a) The phase plane portrait, (b) the power spectrum and (c) snapshots for $H(X)$ and $Q(X)$ for the NSW solution obtained in case A for $R = 32$, $5000 \leqslant t \leqslant 6000$. The snapshots for H and Q shown in (c) is for $t = 6010$ at the time difference of $\Delta t = 10$. The fact that Q changes its sign in the trough in front of the largest hump is clearly seen in all of the snapshots.

within region II. We note that these replicating were first found for the BE by Salamon et al. [5] and later verified by Oron and Gottlieb [16].

In addition to the waveforms described above, there exists a γ_1-type NSW (shown by error bars with black squares) which appears in the vicinity of the lowest TW at $\varepsilon \approx 0.00425$. This point is within region IV and may be reminiscent of the γ_1-branch of TW going through IP found by Scheid et al. [20]. Thus, we conjecture that the γ_1-branch found by Scheid et al. [20] is unstable. We recall that a similar abrupt termination of the γ_1-branch is found in case A beyond $R = 7.6$ corresponding to their $Re = 4.9$.

The amplitudes of the TW solutions of Eqs. (2) and (3) closely follow the amplitudes of the solutions for the Benney equation, as found by Oron and Gottlieb [16,17] and shown in Fig. 3 by white circles. The former are consistently lower than the latter, which in the domain $\varepsilon_2 < \varepsilon < \varepsilon_1$ can be explained by the fact that the solutions of the Benney equation are of the γ_2-type, while those of Eqs. (2) and (3) belong to the γ_1-family. Despite this, the solutions of Eqs. (2) and (3) are in a good agreement with those of Eq. (1) in terms of the amplitude [10] and the topological structure of the wave [16,17], as shown in Fig. 4. Fig. 4 presents several solutions including the normalized interfacial shapes $H(X)$ and the flow rates $Q(X)$, as given by Eqs. (2) and (3) with $R = 3.1$ and various values of ε. A comparison between these and the corresponding interfacial shapes, as obtained from the Benney equation (1), [16] in particular for $\varepsilon = 0.003183$ and $\varepsilon = 0.002$, reveals a very good agreement between them, except for the fact that the solutions for Eqs. (2) and (3) are of the γ_1-type and those of the Benney equation belong to the γ_2-family. Recall that definition of the γ_1- and γ_2-types of waves given in the beginning of Section 5 involves the values $h_{\max}$, $h_{\min}$ and h_N which do not describe the wave shape by themselves. The wave shapes may be very similar each to other topologically, however the corresponding waves may belong to different types due to a little shift in the vertical direction. Figs. 20 and 21 show the wave evolution in the phase plane and the temporal power spectra of the solutions for Eqs. (2) and (3) presented in Fig. 4. The solution complexity grows with decreasing ε from a simple elliptical phase plane for a γ_1-type TW, Fig. 20(a), which further loses symmetry, Fig. 20(b). The γ_2-type TW, Fig. 20(c), incorporates an additional wave or circularity, as was shown in case A, see Fig. 12(b). We note that the phase plane portraits, Figs. 20(d), (e) and the power spectra, Figs. 21(d), (e), of the replicated waves in region V are very similar each to other and to the corresponding γ_1-type TW in region II.

Comparing between the solutions obtained here and the TW solutions found [20] and shown there in Fig. 4, both for Eqs. (2) and (3), we note that the TW solutions [20] presented there in Fig. 4a–c for $k = 0.0256$, 0.0169 and $k = 0.0128$, respectively, agree well with the corresponding (via Eq. (28)) flows we obtain for $\varepsilon = 0.00748$, 0.00494 and 0.00374, respectively. However, our solution for $\varepsilon = 0.002456$ is found to be an NSW, shown in Fig. 22 by its phase plane portrait, and not TW, as that displayed [20] in Fig. 4d obtained for $k = 0.0084$. Thus, while we have not performed a detailed analysis of attraction domains at $\varepsilon = 0.002456$, we conjecture that the γ_2-type TW obtained [20] is unstable.

2. Non-stationary wave solutions

The non-stationary solutions found in case B include three types: (i) NSW corresponding to an unstable γ_1-type TW, $\varepsilon = 0.004$, indicated in Fig. 3 by a bar with black squares; (ii) NSW corresponding to an unstable γ_2-type TW, $\varepsilon = 0.0035, 0.003$ and 0.002456, all indicated in Fig. 3 by bars with black triangles; and (iii) NSW that switches between both the γ_1- and γ_2-waves, $\varepsilon = 0.0033$ and $\varepsilon = 0.0028$, both indicated in Fig. 3 by bars with $\times$. A mixed NSW that switches between γ_1- and γ_2-types waves is depicted in Fig. 23 by its phase plane portrait and power spectrum. A γ_1-type NSW is shown by its phase plane portrait in the lower panel of Fig. 24, whereas a γ_2-type NSW is presented by its phase plane portrait and power spectrum in Fig. 22. We note that all three types of the NSW flows portray the same power spectrum which contains a noisy variability about the harmonic peaks which is indicative of quasiperiodic tori. Furthermore, we recall that a decrease in ε corresponds to increased nonlinearity. Thus, NSW phase plane portraits become denser and their corresponding spectra become wide banded.

We find that the γ_2-type NSW for $\varepsilon = 0.0035$ and $\varepsilon = 0.002456$ agree well with the corresponding γ_2-type NSW of the BE that were depicted [17], Fig. 4(d3) there for $\varepsilon = 0.003394$, and Fig. 5(g), [16] for $\varepsilon = 0.002466$. The NSW solution for $\varepsilon = 0.003394$ was shown to be a quasiperiodic torus [17] via analysis of the corresponding reduced-order dynamical system in the polar representation. Thus, while we cannot rule out existence of chaotic NSW flows in WRIBL Eqs. (2) and (3), the NSW solutions noted above appear to be quasiperiodic. We also note that the variation range of H for NSW solutions of Eqs. (2) and (3) shown by the bars differ from that of the BE, Eq. (1) shown by the white diamonds representing only the maximal value of H.

We comment that Scheid et al. [20] documented the γ_1-type TW for $\varepsilon < 0.004$ in the BE. However, the numerical investigation [9,10] revealed only TW and NSW of the γ_2-type. This result strengthens our previous conjecture that the γ_1-type TW branch in the region $\varepsilon < 0.004$ is indeed unstable in both BE and WRIBL equations.

3. Coexisting solutions

As already noted above, Eqs. (2) and (3) exhibit coexistence between various types of solutions in case B, as well as in case A. However, unlike case A, where coexistence is found only between two types of TW flows, see Fig. 18, the coexistence in case B is found also between the γ_2-type TW with an NSW depicted in Fig. 24 for $\varepsilon = 0.004$ by their evolutions in the phase plane. Fig. 25 presents the coexisting TW flows of the γ_1- and γ_2-families for $\varepsilon = 0.00425$ via

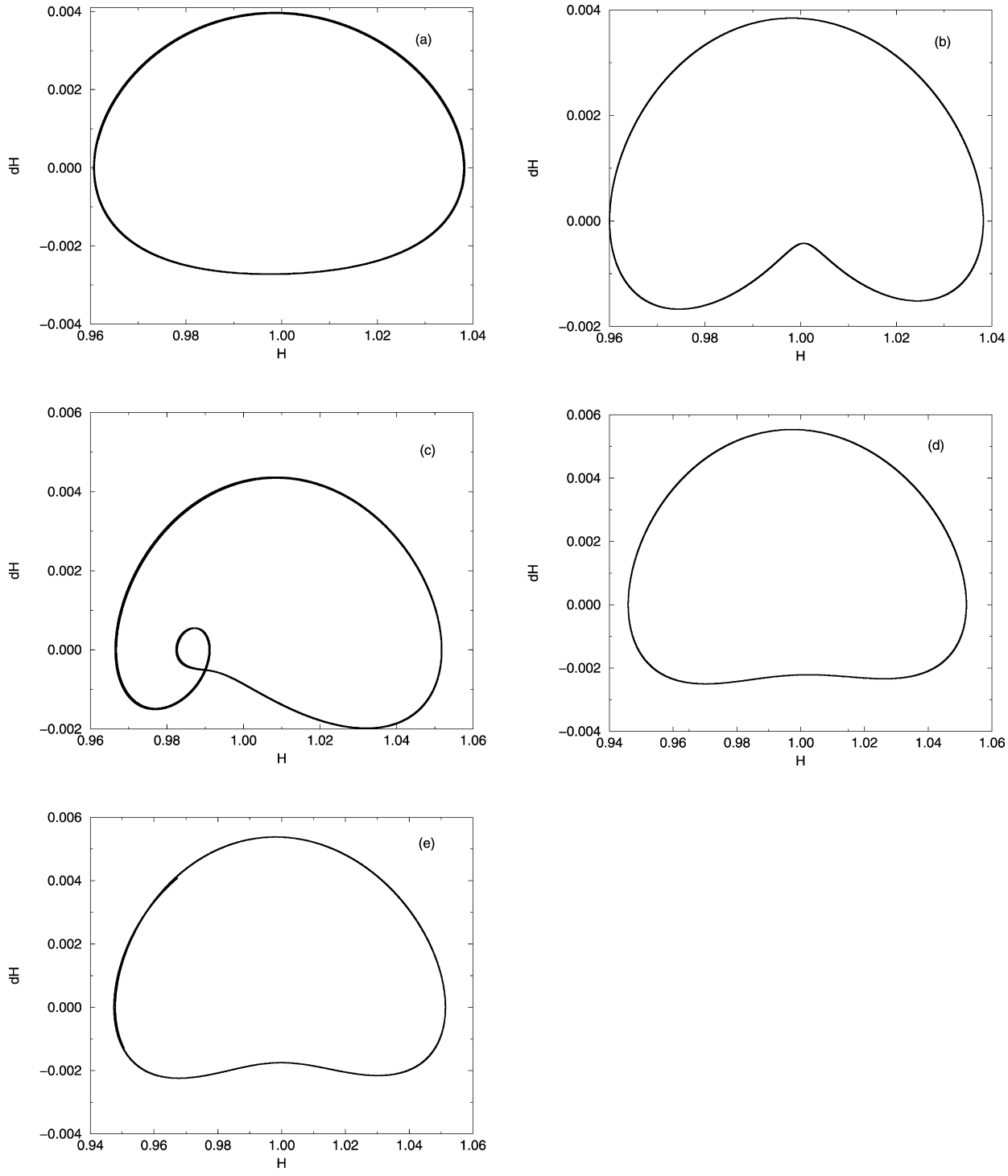

Fig. 20. Phase plane portraits of the TW flows shown in Fig. 4, as obtained from Eqs. (2) and (3). (a) $\varepsilon = 0.0075$ for $3500 \leqslant t \leqslant 4000$, (b) $\varepsilon = 0.004775$ for $4500 \leqslant t \leqslant 5000$, (c) $\varepsilon = 0.003394$ for $3500 \leqslant t \leqslant 4000$, (d) $\varepsilon = 0.003183$ for $38\,000 \leqslant t \leqslant 40\,000$, (e) $\varepsilon = 0.002$ for $38\,000 \leqslant t \leqslant 40\,000$.

their interfacial wave shapes and flow rate distributions along with their phase plane portraits. We note the similarity between the γ_1- and γ_2-types TW coexistence of case B, Fig. 24, and that of case A, Fig. 18.

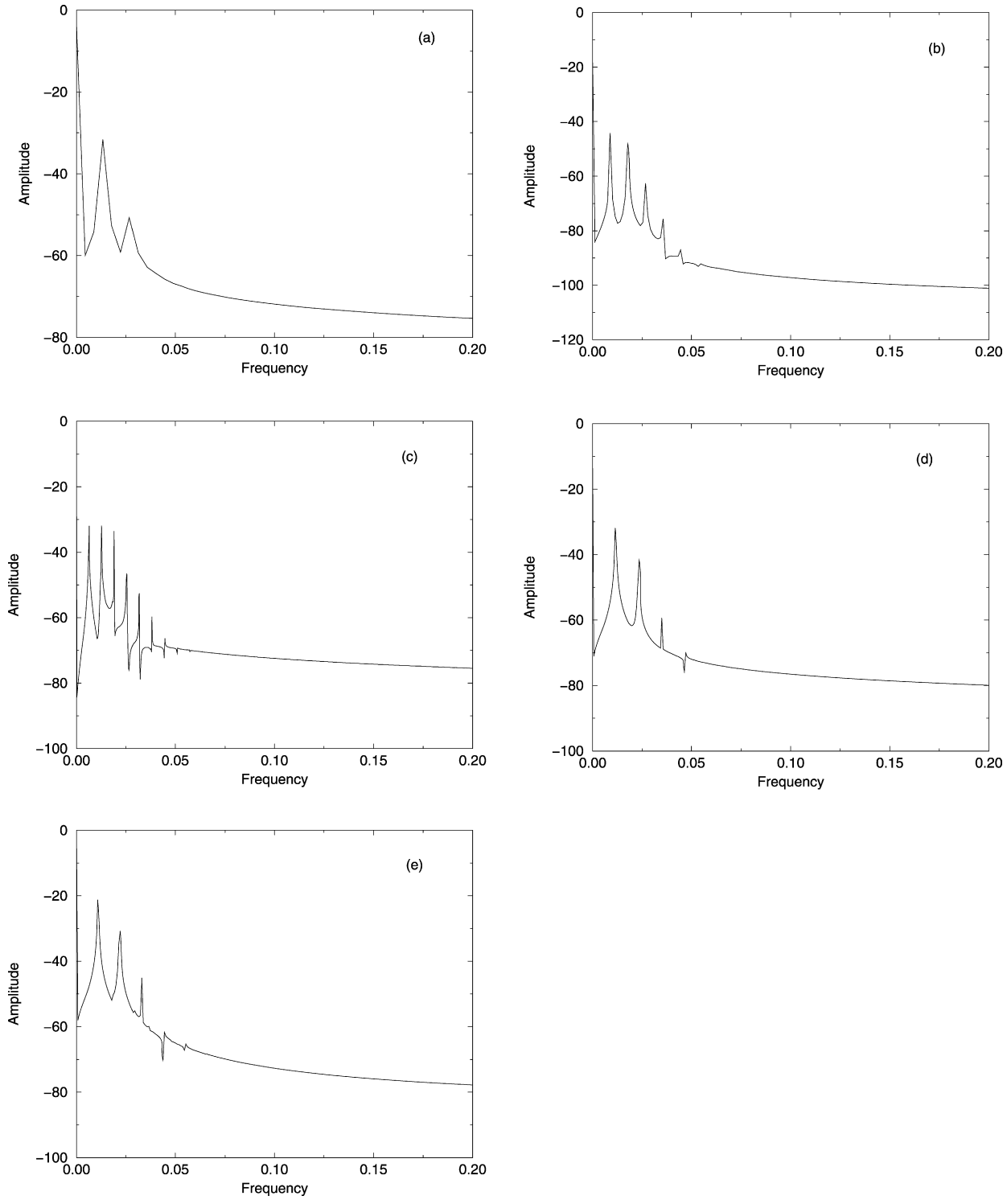

Fig. 21. Power spectra of the temporal evolution of the TW flows shown in Fig. 4 as obtained from Eqs. (2) and (3) for the time ranges indicated in Fig. 20. (a) $\varepsilon = 0.0075$, (b) $\varepsilon = 0.004775$, (c) $\varepsilon = 0.003394$, (d) $\varepsilon = 0.003183$, (e) $\varepsilon = 0.002$.

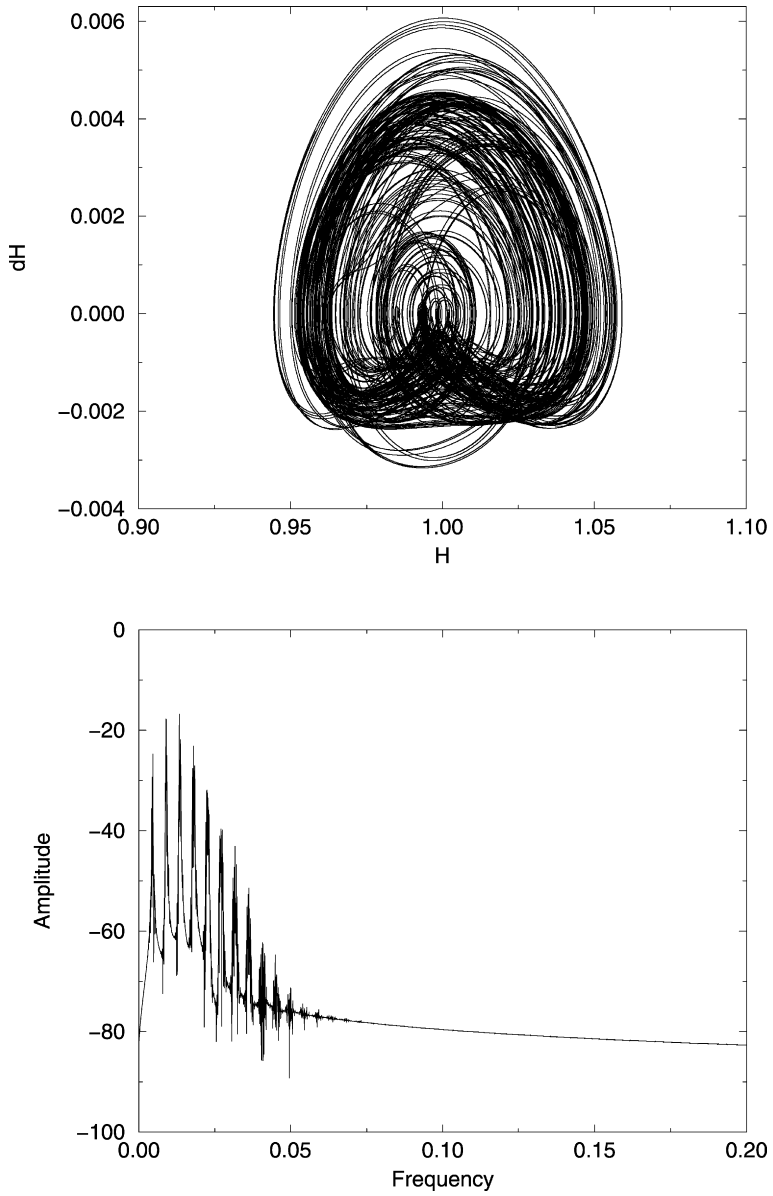

Fig. 22. The upper panel – the phase plane portrait of the solution for Eqs. (2) and (3) in case B for $\varepsilon = 0.002456$ for $40\,000 \leqslant t \leqslant 60\,000$. This solution corresponds to the same parameter values as the TW solution presented in Fig. 4d, [20]. The lower panel: the power spectrum of the temporal evolution in this range.

C. *Cases C and D*

In addition to cases A and B discussed above, we investigate the bifurcation structure of two more cases, namely case C, where $R = 19$, $W = 1000$, and case D, where $R = 32$, $W = 1000$. These cases are similar to case B in the sense that the values of R and W are fixed, while the value of ε varies. The results are presented in Fig. 26. Both of the cases display the emergence of the γ_1-type TW emanating from the stability threshold, as it took place in cases A and B. Unlike in those cases where the exchange between the γ_1- and γ_2-types TW with a coexistence region took place, the γ_1-branch now ceases and gives rise to various types of NSW alternating with windows of γ_2-type TW. Another distinctive feature of cases C and D, as compared with case B, is significantly higher normalized wave amplitudes than in the latter. In cases C and D they can reach values of 1.5 and 2.0, respectively, as compared with 1.05 in case B, which is related to significantly higher values of the Reynolds number.

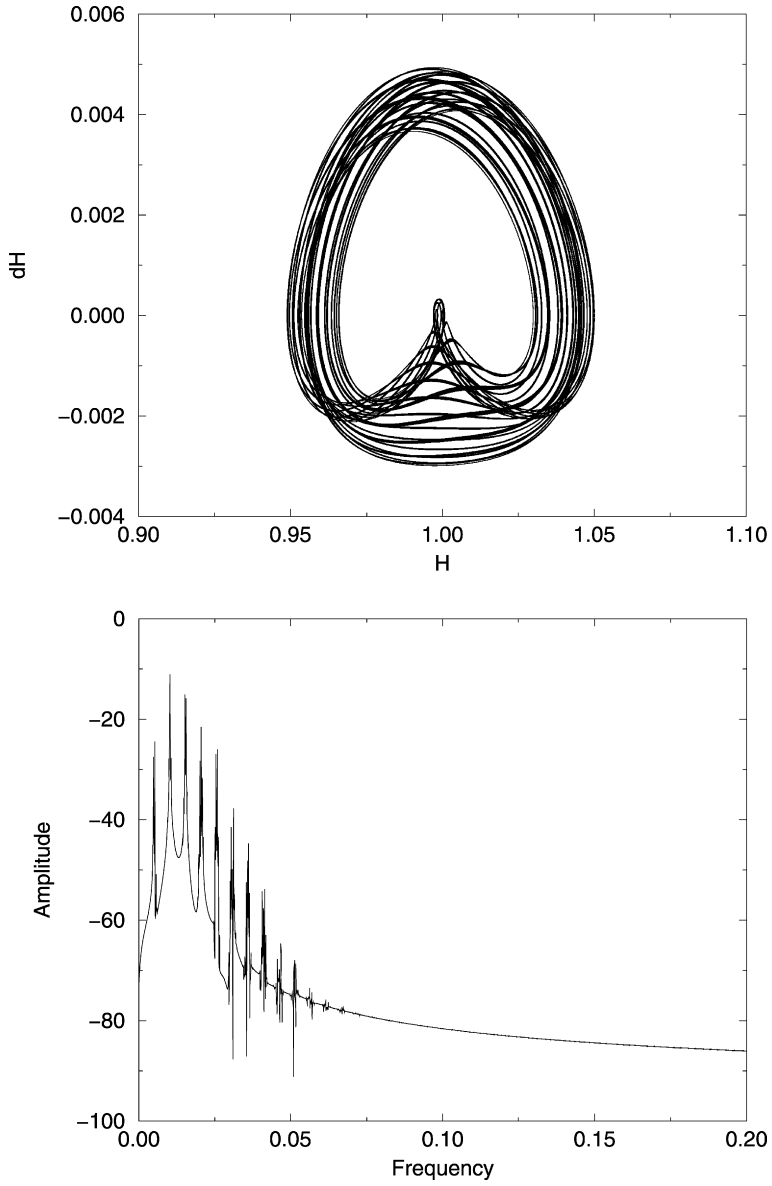

Fig. 23. The upper panel – the phase plane portrait of the solution for Eqs. (2) and (3) in case B for $\varepsilon = 0.0028$ for $35\,000 \leqslant t \leqslant 50\,000$. The lower panel: the power spectrum of the time evolution. The solution shown here is an NSW switching between the γ_1- and γ_2-type waves.

We note that the mixed type of NSW that switches between both γ_1- and γ_2-waves, see Fig. 26, was found close to the transition from γ_1- to the γ_2-waves, whereas this type of mixed NSW was found in case B only for low values of ε, see region V in Fig. 3. These more complicated wave forms, which have been documented in a similar Kuramoto–Sivashinsky system analytically [42,43] and numerically [44], may indicate a tertiary bifurcation depicting a transition to a high-order torus or temporally chaotic solution which remains still unresolved using this type of numerical investigation. Furthermore, this generic secondary and tertiary bifurcation structure has recently been determined both analytically and numerically in the Benney equation for case B, by Gottlieb and Oron [17] where the NSW solution was determined to be a quasiperiodic torus by periodicity of its low-order modal projection. An additional indirect validation of quasiperiodic γ_2-type NSW, was numerically determined by the sensitivity to initial conditions of a temporally-modulated perturbation of the Benney equation [16,17].

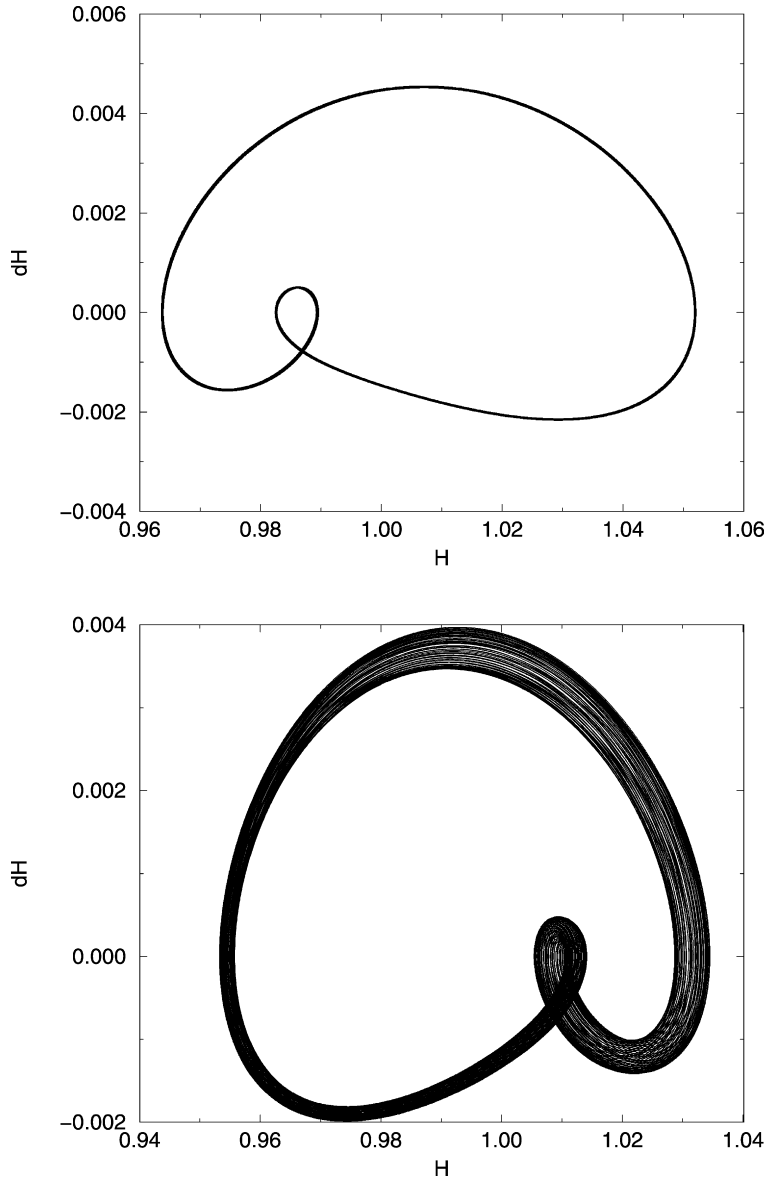

Fig. 24. Coexisting solutions in case B for $\varepsilon = 0.004$. The upper panel – the γ_2-type TW solution, the lower panel – the NSW solution of the γ_1-type, both represented by their phase plane portraits for $14\,000 \leqslant t \leqslant 16\,000$.

7. Emergence of reverse flow

The loss of positivity for Q reported in Section 6(A3) always occurs in the wave trough $h \approx h_{\min}$ corresponding to the minimum of Q. Note that the locations of these minima are linked via Eq. (10) for TW, see for example Fig. 15(d) and 15(e), and this relationship is found to be observed even for NSW. This implies that the flow field displays a domain where a spontaneous return flow, against gravity, takes place. The negative sign of Q reveals that in the corresponding cross-sections of the film the volumetric flow rate entrained in the return flow against gravity, is larger than that in the direction of gravity. The formation of return flow can take place in two possible ways: (i) via the emergence of large-scale vortices of recirculating flow; (ii) via a continuous deformation of the fluid velocity profile.

Wasden and Dukler [45] solved the Navier–Stokes equations and found that in the domain of large Reynolds numbers, i.e. $R = 330$ corresponding to their $Re = 880$ (note a difference in definitions of the Reynolds numbers),

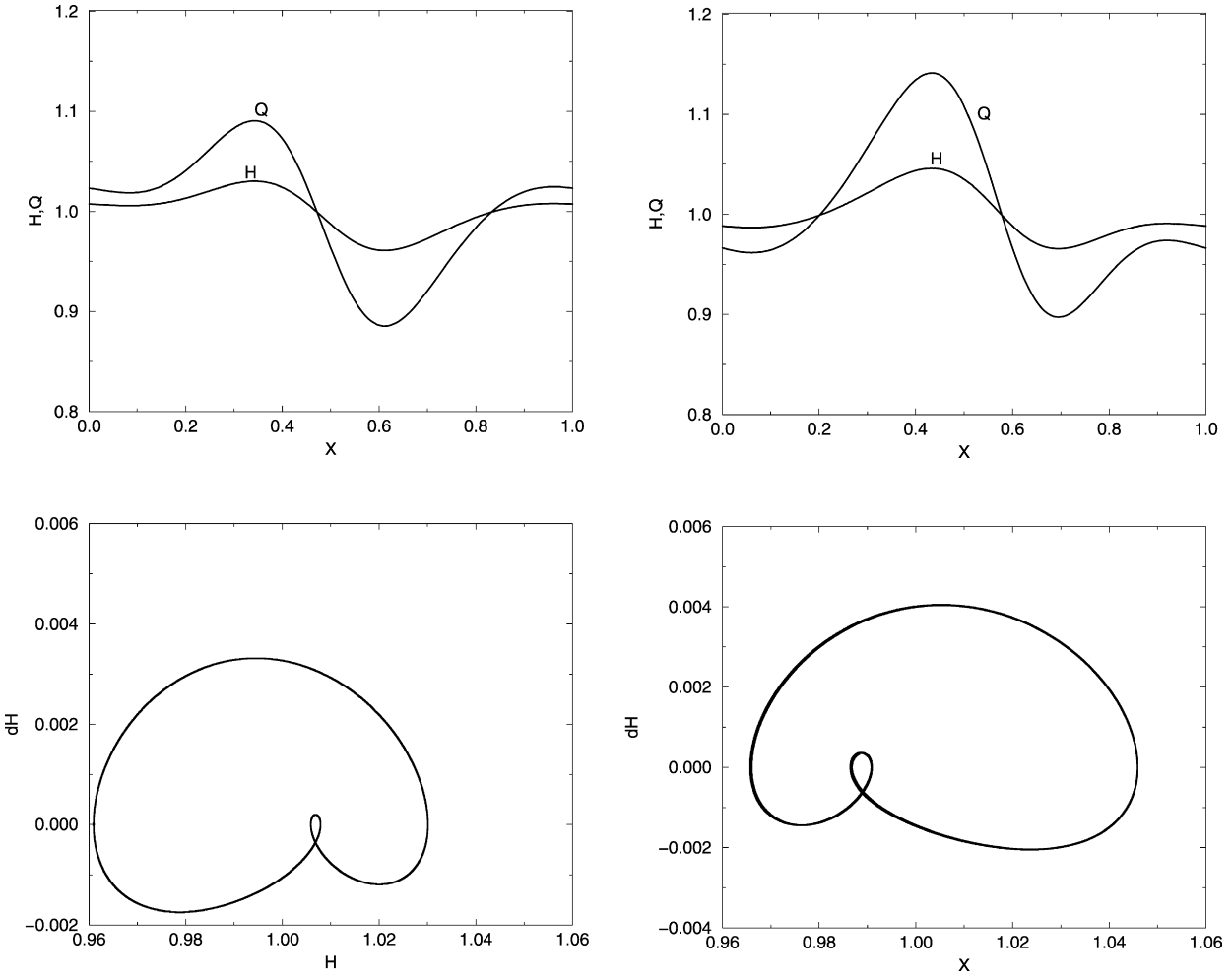

Fig. 25. Coexisting TW solutions in case B for $\varepsilon = 0.00425$. The left panel – the γ_1-solution $H(X)$, $Q(X)$ and its phase plane portrait for $2500 \leqslant t \leqslant 3000$; the right panel – the γ_2-solution $H(X)$, $Q(X)$ and its phase plane portrait for $24\,000 \leqslant t \leqslant 30\,000$.

a recirculating vortex in the moving frame of reference attached to the wave, emerges in the case of waves with large amplitude. The enhancement of heat and mass transfer rates was attributed to this recirculating flow [46]. Vortex solutions are legitimate solutions for the Navier–Stokes equations [45,46].

Formation of the areas with reverse flow was found by Malamataris et al. [6] in their investigations of externally perturbed film flows on slightly inclined planes. Solving numerically the Navier–Stokes equations for moderate Reynolds numbers and small Weber numbers they found that for low-frequency disturbances a reversal flow domain can emerge near the wall in the region of the depression preceding the large-amplitude wave. This reversal flow was shown there to evolve continuously from the domain of the parabolic velocity profile. This scenario cannot be ruled out for the longwave theory underlying Eqs. (2) and (3). It is worthwhile noting that reverse flows were observed in numerical computations based on the Navier–Stokes equations solved for both inclined and vertical planes [6–12,47]. Experimentally, reverse flows were observed by Tihon et al. [47] for film flows on planes slightly inclined with respect to horizontal and subjected to inlet disturbances of controlled frequency. Recently, Scheid et al. [48] reproduced the CFD results by Malamataris et al. [6] by applying AUTO software to determine TW solutions for a second-order and a modified second-order WRIBL equations. They reconstructed the velocity field and showed that a counterflow indeed occurs below the depression in front of a large hump.

As noted in Section 6(A3), the minimal value of $Q(X)$ vanishes at $R \approx 17$. Thus, in case A Eqs. (2) and (3) exhibit flow reversal for $R > 17$, where $Q(X)$ is negative for a certain range of X. Fig. 1 displays the line separating between

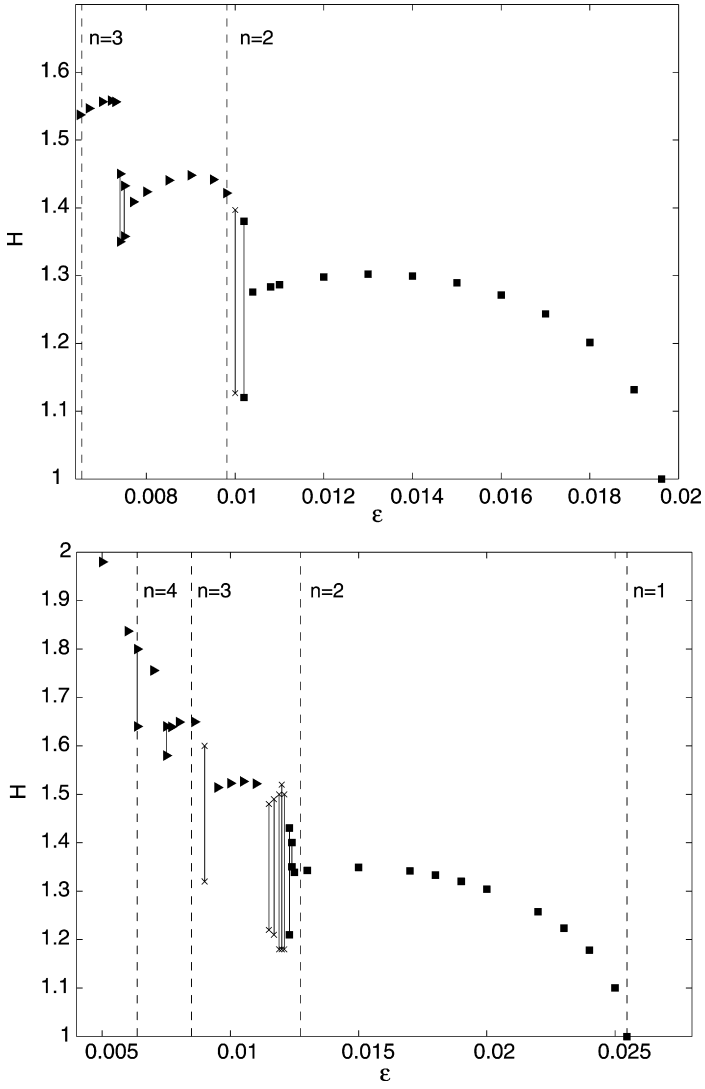

Fig. 26. Bifurcation diagrams in case C: $R = 19$, $W = 1000$ (upper panel) and $R = 32$, $W = 1000$ (lower panel). In both graphs, the legend is identical to that of Fig. 3.

the regions II and III corresponding to positive and negative values of Q, respectively. We restrict our computations to the region of $\varepsilon > 0.03$ where the accuracy of the computation is warranted for a chosen number of grid points, see Section 4. This value of ε corresponds to six linearly unstable modes. Fig. 19(c) depicts several snapshots of the solutions for H and Q for $R = 32$ in case A. As mentioned earlier, the solution in this case represents a NSW and several observations are in order. First, in spite of the fact that Eq. (10) does not follow from Eqs. (2) and (3) for a NSW, the shapes of both Q and H vary coherently. Second and very important, the domain of reverse flow that can be detected here by the fact that Q changes its sign, emerges here for a NSW. We note that this phenomenon cannot be determined by analysis of equilibrium solutions in a TW reference frame, and to our knowledge, has not been reported in any of the CFD or experimental papers that have documented existence of NSW. Finally, the reverse flow can emerge not only in a trough in front of the largest hump but also in the trough located farther from it, as in some snapshots in Fig. 19(c) shown here.

Fig. 27 displays the normalized wave height $\Delta H = (h_{\max} - h_{\min})/h_N$ of the TW flow $H(X)$ along the line separating between regions II (positive Q) and III (negative Q) shown in Fig. 1, as a function of the Reynolds number R. The values of ΔH are computed from the corresponding solutions of Eqs. (2) and (3). Fig. 27 shows that the

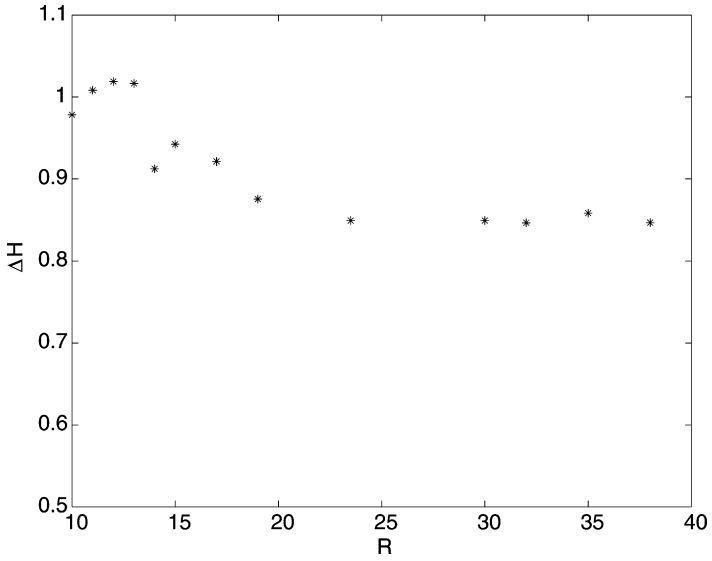

Fig. 27. The normalized wave height $\Delta H = (h_{\max} - h_{\min})/h_N$ of the TW flow $H(X)$ along the line separating between regions II (positive Q) and III (negative Q) shown in Fig. 1, as a function of the Reynolds number R. Along this line the local volumetric flow rate q vanishes. The values of ΔH are computed from the corresponding solutions of Eqs. (2) and (3).

value of ΔH varies slightly between 0.8 and 1.0 over the wide range of $14 \leqslant R \leqslant 38$. Thus, we observe that for $W = 1000$ reverse flow solutions, i.e., with $Q < 0$, emerge for flows with the wave height exceeding a critical value $\Delta H \approx 0.95$.

To determine whether the same effect of the loss of positivity for the volumetric flow rate takes place also for the solutions of the Benney equation slightly before their blowup, we have computed the partial volumetric flow rate determined by the function

$$\hat{q}(x, Y, t) = \int_0^Y u(x, y, t)\, dy = \psi(x, Y, t), \tag{29}$$

where $0 \leqslant Y \leqslant h$, $\psi(x, y, t)$ is the streamfunction of the flow, and $\widehat{q}(x, t; Y = h) = q(x, t)$. The selected test case was that of $R = 7.2$ in case A, i.e. slightly preceding the blowup [16]. The main result of this inquiry is that $\widehat{q}(x, t; Y)$ is positive for all x, t and $Y > 0$, and, is also a monotonically increasing function of Y. This precludes the emergence of closed streamlines and, in particular, that of return flow.

We extend our investigation of the loss of positivity for q to the general case of $W = 1000$. The results are presented in Fig. 1 as a curve in the $\varepsilon - H$ plane marked with black circles that represents a border line between region II of positive Q (to the left of this curve) and region III of negative Q (to the right of the curve), where Eqs. (2) and (3) display reverse flow. Although we have not continued this curve into the domain of larger R, we conjecture that similarly to the behavior of the blow up curve of the Benney equation (bounded solutions above it and unbounded solutions below it) marked with black triangles [16], this curve may finally approach the Hopf bifurcation curve $n = 1$.

Fig. 28 shows the details of the flow in case A with $R = 5$. The flow regime here is TW of the γ_1-type and the wave shapes for $H(X)$ and $Q(X)$ are depicted in the lower panel. The flow rate $Q(X)$ is found to be positive everywhere in the periodic domain and the profiles of the instantaneous streamwise component of the velocity field u, shown in the middle panel, are positive for all y, $0 < y < h$. The upper panel presents a streamline map of the flow at the time corresponding to the solution of Eqs. (2) and (3) shown in the lower panel. The direction of the flow is from the left to the right.

A qualitatively different situation corresponding to the flow in case A with $R = 21$, is presented in Fig. 29. The flow in this case is TW of the γ_2-type, and the wave shapes $H(X)$ and $Q(X)$ are shown in the lower panel. The flow rate $Q(X)$ is found to be negative in the narrow domain indicated by A there. The instantaneous velocity component u is depicted in the middle panel as a function of y, $0 < y < h$, at ten different locations, with curve 1 corresponding to

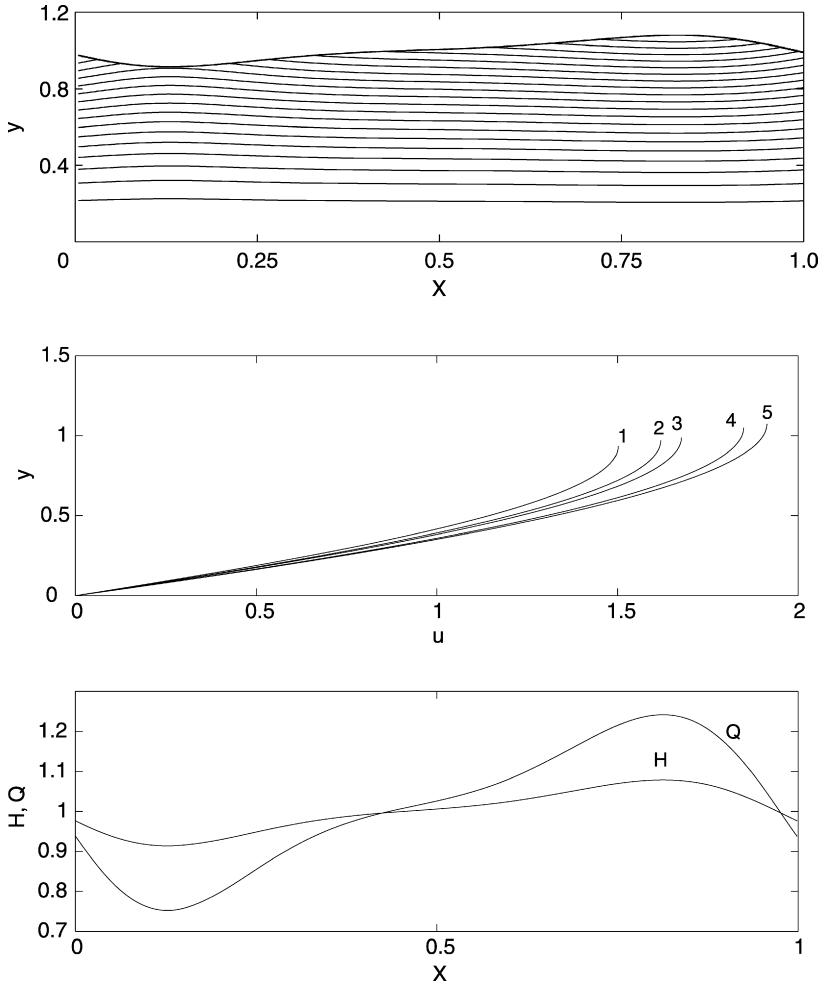

Fig. 28. The streamline map (upper panel), profiles of the instantaneous dimensionless streamwise velocity component u as a function of the transverse coordinate y (middle panel) for various X (curves 1–5 correspond to $X = 0.214$ (minimal value of H), 0.0085, 0.99, 0.686, 0.771 (maximal value of H), respectively), and the profiles of $H = H(X)$, $Q = Q(X)$ (lower panel) corresponding to the traveling wave of the γ_1-type in case A with $R = 5$ at $t = 6000$. The direction of the flow field is from the left to the right.

the minimal value of $Q(X)$ in domain A and the rest corresponding to locations downstream. Curves 1 and 2 show the velocity profiles negative for all y and correspond to reverse flow in the corresponding cross-sections. Curve 3 displays a reverse flow ($u < 0$) with the maximal value of $|u|$ attained in the inner part of the film. Curves 1–3 correspond to the cross-sections within the domain A. Although the velocity profile shown by curve 4 contains a small region adjacent to the wall where backflow takes place, in the rest of the flow field above it the velocity u is positive and the corresponding value of $Q(X)$ is positive. Curves 5–10, are qualitatively similar to those shown in Fig. 28 and correspond to positive values of $Q(X)$. The streamline map in the upper panel displays the region A where reverse flow takes place and the direction of the streamlines is from the right to the left. In the rest of the periodic domain, the flow is from the left to the right and is qualitatively similar to that in Fig. 28. The region A is separated from the rest of the flow field by vertical separatrices. As the solution shown here is TW, the entire picture is translated with time from the left to the right.

It is important to emphasize that the velocity component normal to the flow direction at the edge of a vortex becomes large with respect to the streamwise component of the velocity field. Therefore, the emergence of vortices is beyond the range of applicability of the longwave theory. In the latter, the ratio between the normal and streamwise components of the velocity field should be small at the order of magnitude of the film aspect ratio, as follows from the mass conservation equation. However, as the computed celerity for $R = 21$ is $c = 0.023$, the emergence of reverse

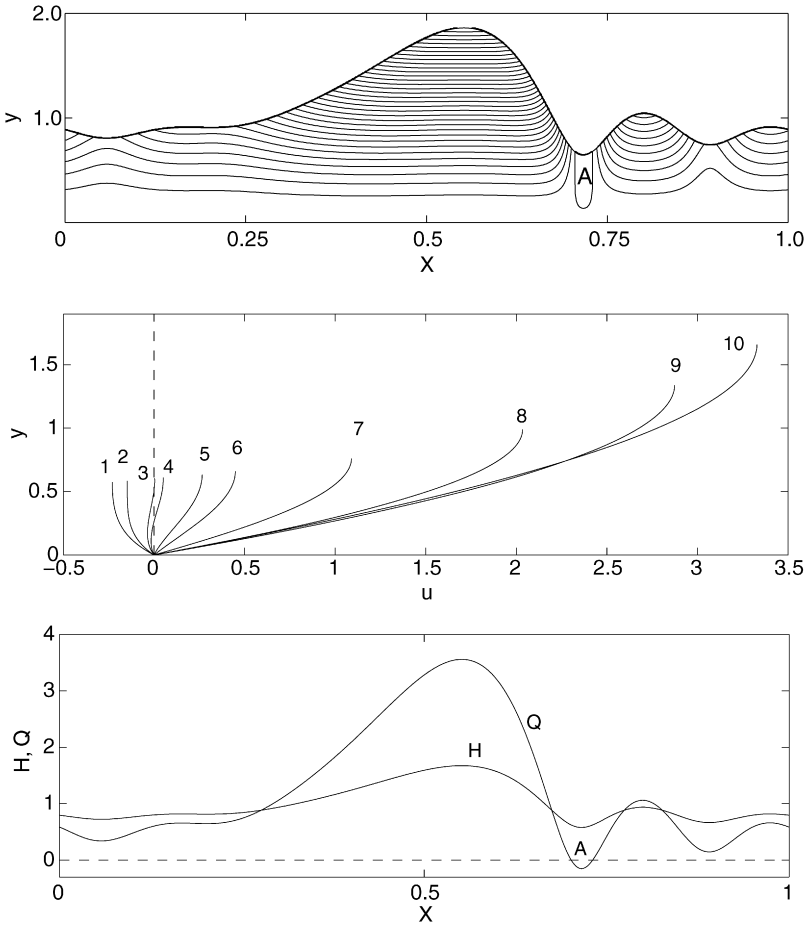

Fig. 29. The streamline map (upper panel), instantaneous profiles of the dimensionless streamwise velocity component u as a function of the transverse coordinate y (middle panel) for various X and the profiles of $H = H(X)$, $Q = Q(X)$ (lower panel) corresponding to the traveling wave of the γ_2-type in case A with $R = 21$. The general direction of the flow field is from the left to the right, but in the region indicated by A the reverse flow takes place.

flow near the wall in the middle panel is qualitatively similar to that computed by Scheid et al. [48] shown there in Fig. 4(c), (d) in the moving frame of reference.

To the best of our knowledge, with the exception of Tihon et al. [47], the emergence of reverse flows in falling films has not been documented experimentally. Therefore, being unable to rigorously disprove its feasibility, we look forward for any experimental confirmation and further theoretical insight into the mechanisms responsible for their emergence for both TW and NSW.

8. Closing remarks

In this paper we have carried out a numerical investigation of the nonlinear dynamics of thin falling films in the context of the first-order weighted-residual boundary-layer (WRIBL) equations derived by Ruyer-Quil and Manneville [24]. These equations, augmented with periodic boundary conditions have been shown to admit solutions of various kinds, among which one finds traveling waves (TW) and several types of aperiodic non-stationary waves (NSW). We note that while TW solutions were documented previously [24,20], the existence of NSW solutions for Eqs. (2) and (3) is first determined in this paper. Furthermore, our numerical investigation of Eqs. (2) and (3) shows that the coexistence of stable TW flows is possible in region III for both cases A and B. This result is similar to that of Scheid et al. [20] for the time-independent WRIBL equations (2) and (3) in case B. Moreover, additional coexisting forms of TW and NSW are also observed here for the first time in the WRIBL equations with periodic boundary

conditions. Based on the results of this investigation of Eqs. (2) and (3), we conjecture that several of the solution branches found in the TW analysis [20] are unstable.

The bifurcation structures of the various cases investigated here possess several common features, as one moves away from the stability threshold of the system: (i) traveling waves of the γ_1-type bifurcate from the stability threshold of the system; (ii) traveling waves of the γ_1-type are replaced by traveling waves of the γ_2-type in the vicinity of the parameter range where the second mode becomes linearly unstable; (iii) the γ_2-type waves then lose stability to a non-stationary flow regime; (iv) when more unstable modes become involved in the film dynamics, an increase in complexity of the spatiotemporal film dynamics occurs. The parameter domain adjacent to the exchange of traveling γ_1-waves by γ_2-waves may contain a subdomain where coexistence between the two types of waves takes place.

We have carried out solution of Eqs. (2) and (3) in several cases corresponding to the experimental observations by Kapitza and Kapitza [34] and Alekseenko et al. [36,37] where the patterns of the falling film surface are spatially periodic, so that periodic boundary conditions are legitimate. In all, but one (Fig. 14, lower panel) of these cases presented in Section 5(3), the topological structure and type of waves (γ_1 or γ_2) is very well reproduced. The waves' celerity obtained from the solution of Eqs. (2) and (3) in the TW cases also compares well with the experimentally measured values. The normalized wave heights, however, obtained from the computations are between 9% and 40% off the measured values, in most of the cases higher than in the experiments. The higher discrepancy between the experiments and theory is presumably due to the absence of dissipative terms in the streamwise direction excluded from first-order WRIBL equations, as compared with second-order equations [24,25,48] and the inability of periodic boundary conditions to reproduce upstream temporal disturbances. We have also carried out a comparison between the solutions of Eqs. (2) and (3) and the numerical solutions of the Navier–Stokes equations obtained by Ramaswamy et al. [15] and Nosoko and Miyara [9]. We found a good agreement between 3% and 17% off the numerically found values for the amplitudes.

The results of this numerical investigation lead to several open questions that cannot be resolved by this type of analysis: (i) the coexisting γ_1- and γ_2-type TW or the coexisting γ_2-type TW and an NSW, are separated by at least one unstable solution. We conjecture that the former is an outcome of a secondary bifurcation which can explain the steep emergence of the γ_2-type TW branch, Fig. 2 at $R \approx 6.7$, and Fig. 3 at $\varepsilon \approx 0.004$. (ii) Furthermore, based on the similarity between the aperiodic NSW of Eqs. (2) and (3) and that of the BE [17] described in Section 6(B3), we conjecture that these NSW solutions are complex quasiperiodic tori and not chaotic strange attractors.

A comparison of the WRIBL equations with the Benney equation which represents an alternative evolution equation describing the nonlinear dynamics of falling liquid films shows that, although there is a generally good agreement in the amplitudes of traveling wave regimes, there are also several key differences: (i) The first is the difference between the γ_1-type waves bifurcating off the linear stability threshold in the case of Eqs. (2) and (3) and the γ_2-type of the waves described by the Benney equation, Eq. (1). We emphasize that unlike the WRIBL equations, the BE does not reveal any stable γ_1-type waves; (ii) The second and perhaps the most important is the fact the WRIBL equations (2) and (3) have not been found to yield unbounded solutions when solved with periodic boundary conditions. While we cannot prove this statement in the general case, this strengthens the findings [24] that the integral boundary-layer approach does indeed prevent a spurious blowup from which the BE suffers; (iii) The third difference is the loss of positivity of q in the WRIBL equations, which is not observed in the BE, where the volumetric flow rate determined via the local film thickness h remains positive everywhere in the periodic domain at all times. This yields a bifurcation structure that consists of stable, bounded and reverse-flow solutions, see Fig. 1. The latter appear for sufficiently large values of the Reynolds number, which corresponds to an increasing nonlinearity. Unfortunately, we have not been able to determine whether the same phenomena take place for decreasing values of the aspect ratio ε. (iv) Coexisting TW and NSW solutions in the WRIBL equations (2) and (3) were found to correspond to those discovered in the modal projection of the BE. [17] However, the WRIBL equations (2) and (3), admit additional coexisting solutions based on the fundamental, *stable* γ_1-type TW which has not been observed in the BE. To the best of our knowledge, coexisting stable time-periodic and time-aperiodic solutions, γ_1 and γ_2, or γ_2 and NSW, have not been observed in experiments or CFD of thin films. It remains to be seen whether such two-dimensional stable flows can coexist in reality.

Acknowledgements

This research was partially supported by the Israeli Science Foundation founded by the Israel Academy of Sciences and Humanities and by the Fund for Promotion of Research at the Technion. A. O. was also partially supported by the

Technion Vice-President Fund and B. and N. Ginsburg Research Fund. We thank Dr. B. Scheid of Universite Libre de Bruxelles for fruitful discussions and for sharing with us his unpublished research results. We also thank Prof. A. Shavit of the Technion for illuminating discussions on reverse flows, and Dr. L. Ioffe for assistance with spectral analysis. The authors acknowledge Prof. S.V. Alekseenko for generously sharing with us copies of his valuable book. We also acknowledge the suggestions made by the anonymous referees that helped to improve the quality of the paper.

Appendix A

Using the numerically obtained solutions $h(x,t)$, $q(x,t)$ for Eqs. (2) and (3), it is possible to reconstruct the velocity field at the given order of approximation using the following expressions:

$$u(x,y,t) = a_0 f_0 + a_1 f_1 + a_2 f_2 + a_3 f_3 + a_4 f_4, \tag{A.1}$$

where

$$f_i = \left(\frac{y}{h}\right)^{i+1} - \frac{i+1}{i+2}\left(\frac{y}{h}\right)^{i+2}, \quad i = 0, 1, \ldots 4, \tag{A.2}$$

$$a_0 = \frac{3q}{h}, \tag{A.3}$$

$$a_1 = \frac{h}{12}a_0 h_t + \frac{h}{60}a_0^2 h_x - \frac{h^2}{6}a_{0,t} - \frac{h^2}{20}a_0 a_{0,x}, \tag{A.4}$$

$$a_2 = -\frac{h}{9}a_0 h_t + \frac{h}{90}a_0^2 h_x + \frac{h^2}{18}a_{0,t} - \frac{h^2}{30}a_0 a_{0,x}, \tag{A.5}$$

$$a_3 = -\frac{h}{30}a_0^2 h_x + \frac{h^2}{60}a_0 a_{0,x}, \tag{A.6}$$

$$a_4 = \frac{h}{150}a_0^2 h_x - \frac{h^2}{300}a_0 a_{0,x}, \tag{A.7}$$

and

$$a_{0,x} = \frac{3}{h^2}(q_x h - q h_x), \qquad a_{0,t} = \frac{3}{h^2}(q_t h + q q_x). \tag{A.8}$$

These expression were derived by Ruyer-Quil and Manneville [24] for their first-order model equations investigated in this paper. The transverse component of the fluid field v is expressed via u through the continuity equation.

References

[1] A. Oron, S.H. Davis, S.G. Bankoff, Long-scale evolution of thin liquid films, Rev. Mod. Phys. 69 (1997) 931.
[2] D.J. Benney, Long waves on liquid films, J. Math. Phys. 45 (1966) 150.
[3] B. Gjevik, Occurrence of finite-amplitude surface waves on falling liquid films, Phys. Fluids 13 (1970) 1918.
[4] C. Nakaya, Waves on a viscous fluid film down a vertical wall, Phys. Fluids A 1 (1989) 1143, and references therein.
[5] T.R. Salamon, R.C. Armstrong, R.A. Brown, Traveling waves on vertical films: Numerical analysis using the finite element method, Phys. Fluids A 6 (1994) 2202.
[6] N.A. Malamataris, M. Vlachogiannis, V. Bontozoglou, Solitary waves on inclines films: Flow structure and binary interactions, Phys. Fluids 14 (2002) 1082.
[7] D. Gao, N.B. Morley, V. Dhir, Numerical simulation of wavy falling film flow using VOF method, J. Comp. Phys. 192 (2003) 624.
[8] C.D. Park, T. Nosoko, Three-dimensional wave dynamics on a falling film and associated mass transfer, AIChE J. 49 (2003) 2715.
[9] T. Nosoko, A. Miyara, The evolution and subsequent dynamics of waves on a vertically falling liquid film, Phys. Fluids 16 (2004) 1118.
[10] T. Kunugi, C. Kino, DNS of falling film structure and heat transfer via MARS method, Comp. Struct. 83 (2005) 455.
[11] J. Tihon, K. Serifi, K. Argyriadi, V. Bontozoglou, Solitary waves on inclined films: Their characteristics and the effects on wall shear stress, Exp. Fluids 41 (2006) 79.
[12] A. Miyara, Numerical simulation of wavy liquid film flowing down on a vertical wall and an inclined wall, Int. J. Therm. Sci. 39 (2000) 1015.
[13] S.W. Joo, S.H. Davis, Irregular waves on viscous falling films, Chem. Eng. Comm. 118 (1992) 111.
[14] S.W. Joo, S.H. Davis, Instabilities of three-dimensional viscous falling films, J. Fluid Mech. 242 (1992) 529.
[15] B. Ramaswamy, S. Chippada, S.W. Joo, A full-scale numerical study of interfacial instabilities in thin-film flows, J. Fluid Mech. 325 (1996) 163.
[16] A. Oron, O. Gottlieb, Nonlinear dynamics of temporally excited falling liquid films, Phys. Fluids 14 (2002) 2622.

[17] O. Gottlieb, A. Oron, Stability and bifurcations of parametrically excited thin liquid films, Int. J. Bifurcation Chaos 14 (2004) 4417.
[18] A. Pumir, P. Manneville, Y. Pomeau, On solitary waves running down an inclined plane, J. Fluid Mech. 135 (1983) 27.
[19] P. Rosenau, A. Oron, J.M. Hyman, Bounded and unbounded patterns of the Benney equation, Phys. Fluids A 4 (1992) 1102.
[20] B. Scheid, C. Ruyer-Quil, U. Thiele, O.A. Kabov, J.C. Legros, P. Colinet, Validity domain of the Benney equation including Marangoni effect for closed and open flows, J. Fluid Mech. 527 (2005) 303.
[21] S.P. Lin, Finite amplitude side-band stability of a viscous film, J. Fluid Mech. 63 (1974) 417.
[22] A. Oron, O. Gottlieb, Subcritical and supercritical bifurcations of the first- and second-order Benney equations, J. Eng. Math. 50 (2004) 121.
[23] T. Ooshida, Surface equation of falling film flows with moderate Reynolds number and large but finite Weber number, Phys. Fluids 11 (1999) 3247.
[24] C. Ruyer-Quil, P. Manneville, Improved modeling of flows down inclined planes, Eur. Phys. J. B 15 (2000) 357.
[25] C. Ruyer-Quil, P. Manneville, Further accuracy and convergence results on the modeling of flows down inclined planes by weighted-residual approximations, Phys. Fluids 14 (2002) 170.
[26] V.Ya. Shkadov, Wave flow regimes of a thin layer of a viscous fluid subject to gravity, Izv. Akad. Nauk SSSR, Mekh. Zhidk. Gaza 2 (1967) 43. Also, translated in Fluid Dyn. 2 (1970) 29.
[27] H.C. Chang, E.A. Demekhin, D.I. Kopelevich, Nonlinear evolution of waves on a vertically falling film, J. Fluid Mech. 250 (1993) 433.
[28] H.C. Chang, Wave evolution on a falling film, Ann. Rev. Fluid Mech. 26 (1994) 103.
[29] T.B. Benjamin, Wave formation in laminar flow down an inclined plane, J. Fluid Mech. 2 (1957) 554.
[30] C.-S. Yih, Stability of liquid flow down an inclined plane, Phys. Fluids 6 (1963) 321.
[31] G.M. Sisoev, V.Y. Shkadov, A two-parameter manifold of wave solutions to an equation for a falling film of a viscous fluid, Dokl. Phys. 44 (1999) 454.
[32] V.Y. Shkadov, G.M. Sisoev, Waves induced by instability in falling films of finite thickness, Fluid Dyn. Res. 35 (2004) 357.
[33] R.R. Mudunuri, V. Balakotaiah, Solitary waves on thin falling films in the very low forcing frequency limit, AIChE J. 52 (2006) 3995.
[34] P.L. Kapitza, S.P. Kapitza, Wave flow of thin layers of a viscous fluid, Zh. Eksper. i Teor. Fiz. 19 (1949) 105. Also, in: Collected Works, Pergamon Press, New York, 1965, p. 690.
[35] C.E. Lacy, M. Sheintuch, A.E. Dukler, Methods of deterministic chaos applied to the flow of thin wavy films, AIChE J. 37 (1991) 481.
[36] S.V. Alekseenko, V.Ya. Nakoryakov, B.G. Pokusaev, Wave formation on a vertical falling liquid film, AIChE J. (1985) 1446–1460.
[37] S.V. Alekseenko, V.Ya. Nakoryakov, B.G. Pokusaev, Wave Flow of Liquid Films, Begell House, New York, 1994.
[38] J. Liu, J.D. Paul, J.P. Gollub, Measurements of the primary instabilities of film flows, J. Fluid Mech. 250 (1993) 69.
[39] J. Liu, J.P. Gollub, Solitary wave dynamics of film flows, Phys. Fluids 6 (1994) 1702.
[40] J. Liu, J.B. Schneider, J.P. Gollub, 3-dimensional instabilities of film flows, Phys. Fluids 7 (1995) 55.
[41] A. Oron, Nonlinear dynamics of three-dimensional long-wave Marangoni instability in thin liquid films, Phys. Fluids 12 (2000) 1633.
[42] D. Armbruster, J. Guckenheimer, P. Holmes, Heteroclynic cycles and modulated traveling waves in systems with $O(2)$-symmetry, Physica D 29 (1988) 257.
[43] D. Armbruster, J. Guckenheimer, P. Holmes, Kuramoto–Sivashinsky dynamics on the center-unstable manifold, SIAM J. Appl. Math. 49 (1989) 676.
[44] I.G. Kevrekidis, B. Nicolaenko, J.C. Scovel, Back in the saddle again- a computer-assisted study of the Kuramoto–Sivashinsky equation, SIAM J. Appl. Math. 50 (1990) 760.
[45] F.K. Wasden, A.E. Dukler, Numerical investigation of large wave interactions on free falling films, Int. J. Multiphase Flow 15 (1989) 357.
[46] F.K. Wasden, A.E. Dukler, A numerical study of mass-transfer in free falling wavy films, AIChE J. 36 (1990) 1379.
[47] J. Tihon, V. Tovchigrechko, V. Sobolik, O. Wein, Electrodiffusion detection of the near-wall flow reversal in liquid films at the regime of solitary waves, J. Appl. Electrochem. 33 (2003) 577.
[48] B. Scheid, C. Ruyer-Quil, P. Manneville, Wave patterns in film flows: Modelling and three-dimensional waves, J. Fluid Mech. 562 (2006) 183.